J. Fluid Mech. (2018), *vol.* 852, *pp.* 678–709. © Cambridge University Press 2018
doi:10.1017/jfm.2018.553

Drag control in wall-bounded turbulent flows via spanwise opposed wall-jet forcing

Jie Yao[1], **Xi Chen**[1] **and Fazle Hussain**[1,†]

[1]Texas Tech University, Department of Mechanical Engineering, Lubbock, TX 79409, USA

(Received 12 November 2017; revised 30 May 2018; accepted 9 July 2018;
first published online 13 August 2018)

Drag control using a newly developed spanwise opposed wall-jet forcing (SOJF) method is studied via direct numerical simulation of the incompressible Navier–Stokes equations in a turbulent channel flow (at the friction Reynolds numbers $Re_\tau = 180$ and 550). SOJF is characterized by three control parameters: the forcing amplitude A^+, the spanwise spacing λ^+ and the wall-jet height y_c^+ (+ indicates viscous scaling). At $Re_\tau = 180$, notable drag reduction is achieved for wide ranges of A^+, λ^+ and y_c^+, with an optimal drag reduction of approximately 19 % found for $A^+ \approx 0.015$, $\lambda^+ \approx 1200$ and $y_c^+ \approx 30$. The drag reduction results from mergers of numerous low-speed typical individual streaks together by the wall jets, so that the slope of the merged streak envelope and hence the streak strength are reduced below the critical values required for streak instability as well as for transient growth; consequently, the generation of drag inducing near-wall streamwise vortices is suppressed. Through analysis using the FIK identity (Fukagata *et al. Phys. Fluids*, vol. 14 (11), 2002, pp. L73–L76) in combination with the triple decomposition and the spanwise wavenumber spectrum of the Reynolds shear stress, we find that the control significantly decreases skin friction due to the small scale random turbulent structures (from 75 to 23 % for the optimal case), but injects a dominant contribution at the forcing scale (approximately 34 %). As A^+ or y_c^+ increases, the drag reduction degrades due to the downwash near the initiation of the forcing wall jet. The energy input required for the excitation is found to be small, yielding a 17 % net power saving for the optimal control case. To determine the Re dependence of the drag reduction, the control strategy is further validated at a higher $Re_\tau = 550$. If the control parameters are kept the same as at $Re_\tau = 180$ (i.e. $A^+ \approx 0.015$, $\lambda^+ \approx 1200$, $y_c^+ \approx 30$), the drag reduction decreases to 10 %; however, interestingly, with modestly changed parameters ($A^+ \approx 0.018$, $\lambda^+ \approx 1700$, $y_c^+ \approx 50$), drag reduction increases to about 15 %. This additional drag reduction results from the further suppression of turbulent structures in the buffer and log regions. This result, therefore, suggests prospects for drag reduction at even higher Re via a proper choice of the SOJF parameters.

Key words: drag reduction, flow control, turbulent boundary layers

1. Introduction

The ability to control turbulent boundary layers (TBLs) to reduce drag is of great importance for energy saving and hence also for environmental pollution control (Kim 2011). Successful control of TBLs requires a thorough understanding

† Email address for correspondence: fazlehussain@gmail.com

https://doi.org/10.1017/jfm.2018.553 Published online by Cambridge University Press

of the underlying physics. During the past several decades, one major advance in TBL research is the discovery, understanding and documentation of organized coherent structures and their important roles in the near-wall dynamics. It is well known that the near-wall structures are involved in a self-sustained cycle (Hamilton, Kim & Waleffe 1995; Jiménez & Pinelli 1999; Schoppa & Hussain 2002, cited hereafter as SH1): the low-speed streaks are generated via the lift-up effect of faster advecting streamwise vortices leaving streaks as their trails (Butler & Farrell 1993), while the instability/transient growth of low-speed streaks – if sufficiently strong – causes regeneration of streamwise vortices (Hamilton *et al.* 1995, SH1). In general, interrupting any stage of this self-sustaining cycle could result in the suppression of streamwise vortex generation and hence reduction of drag – the current goal of many drag control endeavours.

Based on whether external energy is required to drive the control, drag reduction methods can be grouped into passive and active techniques. As one of the oldest and most highly investigated passive drag control methods, riblets have been shown to yield about 5%–7 % drag reduction in full-scale trials (Bechert *et al.* 1997). However, its continuous sustenance in practical applications is still an unresolved issue. Recently, other passive drag reduction strategies have been conceived and developed. For example, superhydrophobic surfaces have been reported to yield up to 50 % and 75 % drag reduction in laboratory turbulent channel (Rothstein 2010) and boundary layer (Park *et al.* 2014) experiments, respectively. Despite these remarkable results, the approach still has not yet evolved into a practical means, mainly because the superhydrophobic surfaces are highly vulnerable to high pressure and high shear rate in practical environments (Checco *et al.* 2014; Rastegari & Akhavan 2018). On the other hand, active control methods (Choi, Moin & Kim 1994; Kim & Bewley 2007; Chung & Talha 2011; Deng & Xu 2012; Mamori, Iwamoto & Murata 2014) usually require highly sophisticated closed-loop control strategies, often involving intrusive sensing and electro-mechanical flow actuations. The recently proposed streamwise travelling wave-based (also spanwise wall oscillations) control strategies are fascinating (Jung, Mangiavacchi & Akhavan 1992; Choi, Xu & Sung 2002; Quadrio, Ricco & Viotti 2009; Quadrio 2011; Agostini, Touber & Leschziner 2014; Yakeno, Hasegawa & Kasagi 2014), where significant drag reductions (as much as 45 % at small Re) are achieved. However, whether effective drag reduction can be obtained at practical, high Re remains unclear. Early studies (Choi *et al.* 2002; Ricco & Quadrio 2008; Touber & Leschziner 2012) show a rapid decay of drag reduction with increasing Re, suggesting no more than 7 % drag reduction at $Re = 10^6$ – not accounting for the energy cost. On the other hand, Gatti & Quadrio (2016) recently performed a detailed study of the Re effect in turbulent channel flows up to $Re_\tau = 1000$, and asserted that a 30 % drag reduction is still possible for airplane at flight Re values. To summarize, a controlling strategy with effective drag reduction and practical applicability remains a challenge.

We seek large-scale active control methods which are robust and independent of instantaneous flow dynamics (hopefully without any sophisticated sensing as well as mechanical actuation). Schoppa & Hussain (1998) (hereafter referred to as SH2) developed a conceptually simple open-loop control strategy for TBLs. By imposing large-scale counter-rotating streamwise swirls with a relatively small excitation amplitude (approximately 6 % of the free-stream velocity), they computationally obtained 20 % drag reduction in a turbulent channel at $Re_\tau = 104$. Recently, Canton *et al.* (2016*a*) found SH2's method only yields a transient drag reduction and instead recreated a large-scale swirl control method by numerically introducing a

https://doi.org/10.1017/jfm.2018.553 Published online by Cambridge University Press

volume forcing. The maximum drag reduction was found to be 18 % at $Re_\tau = 180$, with the optimal spanwise spacing $\lambda^+ = 1200$. (Hereafter, the superscript + indicates non-dimensionalization in wall units of the uncontrolled flow: e.g. $y^+ = yu_{\tau,0}/\nu$, where ν is the kinematic viscosity, $u_{\tau,0} = \sqrt{\nu\, \mathrm{d}U/\mathrm{d}y|_w}$ is the friction velocity for the uncontrolled flow and $\mathrm{d}U/\mathrm{d}y|_w$ is the gradient of the streamwise mean velocity at the wall.) More recently, Canton *et al.* (2016*b*) found that the drag reduction decreases with increasing *Re* and becomes zero at $Re_\tau = 550$; they suggested that the control swirls centred at the half-channel height fail to penetrate the viscous sublayer at high *Re* and are hence unable to affect the near-wall regeneration cycle.

Contrary to the implications of Canton *et al.*'s (2016*b*) findings, it turns out that the concept of SH2's large-scale control strategy is indeed robust and operative. SH2's key point was that an appropriate introduction of large-scale swirls (easily achieved by opposing wall jets) can merge multiple streaks together into a larger streak envelope so that its strength (quantified by the streak flank angle $\tan^{-1}(|\omega_y|/|\omega_z|)$) is below the critical value for streak instability/transient growth – hence leading to the suppression of the generation of streamwise vortices, clearly producing drag reduction (SH1). In fact, using vortex generator jets (Iuso *et al.* 2002) or plasma actuators (Li *et al.* 2014; Thomas *et al.* 2016), there have already been several experimental attempts to explore the large-scale control strategies of SH2 in turbulent channel and boundary layer flows, and notable drag reductions were found at moderate *Re*. In addition, a net power saving of the order of 10 % was also found for turbulent pipe flow by forcing steady large-scale swirls (Willis, Hwang & Cossu 2010). According to our recent study (Yao *et al.* 2017), the negative results found by Canton *et al.* (2016*b*) arose from their selection of the channel centre height as the fixed value for the location of the control swirl centres. However, this choice was not suggested as a requirement in SH2 in their proof-of-principle paper; also, when applied to TBLs, for example, there would be no channel height and the height of the control flow obviously should be specified in terms of y^+.

In Yao *et al.* (2017), we validated SH2's concept for high *Re* using the near-wall spanwise opposed wall-jet forcing (SOJF). The goal of the present paper is to place the SOJF drag reduction technique on a sound scientific foundation by examining and delineating the detailed mechanisms involved and their efficacy, from both statistical and dynamical perspectives. Specifically, the effects of selecting different combinations of the control parameters on the drag reduction performance are studied, together with the estimation of the control energy input and net energy saving. The contributions of the skin friction from different scales are analysed using the triple decomposition and the FIK identify (Fukagata, Iwamoto & Kasagi 2002). Moreover, coherent structures are investigated to understand the physical mechanism of drag reduction, and possible *Re* effects.

Note that the current SOJF is still an idealized forcing, employed to mimic the generation of streamwise swirls obtained by either colliding wall jets (Iuso *et al.* 2002) or plasma actuators (Li *et al.* 2014; Thomas *et al.* 2016). Adding a body force in the incompressible Navier–Stokes equation to mimic the Lorentz force has been applied before (Berger *et al.* 2000; Mahfoze & Laizet 2017). Although more sophisticated numerical simulation is needed to correctly mimic the Lorentz force of real plasma effects (Corke, Enloe & Wilkinson 2010), large-scale swirls and spanwise variation of the wall shear stress developed by our phenomenological model (2.3) have been found to compare well with the recent experiments by plasma actuators (Li *et al.* 2014; Thomas *et al.* 2016). In this sense, the numerical results in this paper have general relevance and can indeed guide choices of experimental parameter values.

https://doi.org/10.1017/jfm.2018.553 Published online by Cambridge University Press

The paper is organized as follows. Section 2 details the computational set-up and control scheme. Section 3 presents a parametric study for the drag reduction at $Re_\tau = 180$ and identifies the optimal parameters for the maximum drag reduction. Analysis of the detailed flow statistics and elucidation of the underlying dynamics of structures are given in § 4. The efficacy of the control via a discussion of energy input, as well as results for the higher Re_τ (= 550) are presented in § 5. Section 6 summarizes our results.

2. Computational methods and initial set-up

The incompressible Navier–Stokes equations for the velocity and pressure $(\boldsymbol{u}, p)$ are

$$\boldsymbol{\nabla} \cdot \boldsymbol{u} = 0, \tag{2.1}$$

$$\partial_t \boldsymbol{u} + \boldsymbol{u} \cdot \boldsymbol{\nabla} \boldsymbol{u} = -\frac{1}{\rho} \boldsymbol{\nabla} p + \nu \nabla^2 \boldsymbol{u} + \boldsymbol{F}, \tag{2.2}$$

where ν is kinematic viscosity, ρ is density and $\boldsymbol{F}$ is the body forcing. The streamwise, wall-normal and spanwise coordinates are denoted by x, y, z, respectively, and u, v, w are the velocities in these directions. Different from the swirl used in SH2 and Canton *et al.* (2016*a*,*b*), we here apply a near-wall SOJF:

$$F_x = F_y = 0; \quad F_z = A \sin(\beta z) g(y^+), \tag{2.3a,b}$$

where A is the forcing amplitude, $\beta\ (= 2\pi/\lambda)$ is the spanwise wavenumber and $g(y^+)$ is a dimensionless forcing as a function of y. Throughout the paper, we normalize all control parameters in viscous units based on uncontrolled flow: (i) $A^+ = A\nu/u_{\tau,0}^3$; (ii) $\lambda^+ = 2\pi/\beta^+$ $(\beta^+ = \beta\nu/u_{\tau,0})$; and (iii) $y_c^+ = y_c u_{\tau,0}/\nu$. For forcing function $g(y^+)$ in (2.3), we choose the same form as used by SH1

$$g(y^+) = y^+ \exp(-\eta y^{+2}), \tag{2.4}$$

where the decay factor η in the wall-normal direction specifies the wall-jet velocity profile. The function g has its maximum at $y^+ = y_c^+ = 1/\sqrt{2\eta}$, and y_c^+ represents the height of the spanwise wall-jet maximum velocity. Note that in (2.3), g is normalized by its maximum value $g(y_c^+) = y_c^+ \exp(-0.5)$.

Figure 1(*a*) shows the velocity field induced by the SOJF excitation with $A = 0.005$, $\beta = 1$ and $\eta = 18$ in the cross-stream (y–z) plane. Note that the colliding wall jets turn upward and then backward constrained by the upper channel wall and then down back (downwash) toward the originating wall – thus forming the large-scale streamwise control swirls while also squashing the incoming wall jets. These swirls produce near their collision plane a pair of near-wall counter-rotating smaller (secondary) swirls of opposite sense to the primary swirls, which also affect the drag reduction performance. In particular, the tiny secondary swirls prevent the near-wall streaks on either side of the collision plane from merging, actually even strengthening and separating these two adjacent streaks; the resulting instability of these two strong streaks actually plays a role in creating streamwise vortices above the streak envelope. Figure 1(*b*) shows the corresponding spanwise velocity profiles at different spanwise locations; the maximum spanwise velocity is located at y_c, which we use as the height of the wall jet. The profiles near the wall appear qualitatively similar to those generated by plasma actuators (inferred from the control flow vector patterns in Li *et al.* (2014); also, Thomas *et al.* (2016)).

https://doi.org/10.1017/jfm.2018.553 Published online by Cambridge University Press

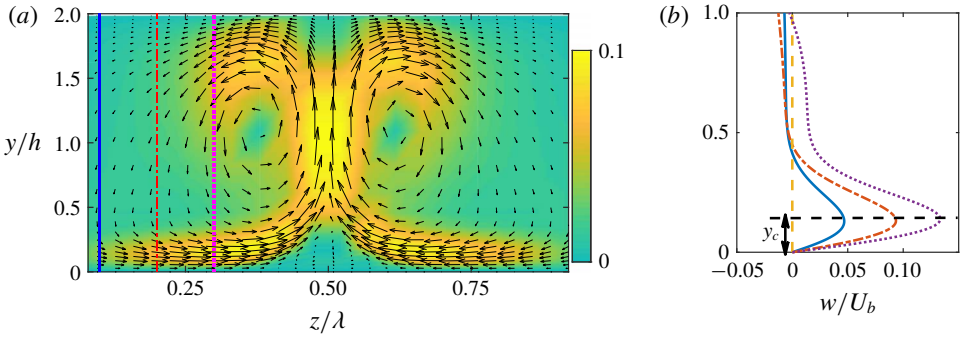


FIGURE 1. (Colour online) (*a*) Vector pattern of induced flow (v, w) in the cross-stream $(y$–$z)$ plane with the colour denoting the velocity magnitude; (*b*) spanwise velocity profile (normalized with the bulk velocity) of the induced wall jet at different spanwise locations: the profiles are taken along the vertical lines shown in (*a*) at $z/\lambda = 0.1$, 0.2 and 0.3.

Re_τ	Re_b	T	$L_x/h, L_z/h$	L_x^+, L_z^+	$N_x \times N_y \times N_z$
			$4\pi, 2\pi$	2262, 1131	$192 \times 129 \times 128$
180	2 800	900	$4\pi, 4\pi$	2262, 2262	$192 \times 129 \times 256$
			$4\pi, 6\pi$	2262, 3393	$192 \times 129 \times 384$
550	10 000	600	$4\pi, 2\pi$	6912, 3456	$512 \times 193 \times 384$

TABLE 1. Details of the numerical discretization employed for the present simulations.

The current simulations of turbulent channel flows are based on the open-source finite difference software 'Incompact3d' (Laizet & Lamballais 2009; Laizet & Li 2011), where periodicity in the streamwise and spanwise directions is imposed, and no-slip and impermeability conditions are applied at the walls. For the spatial derivatives, sixth-order compact schemes are used on a Cartesian grid stretched in the wall-normal direction. The time integration is performed using a low-storage third-order Runge–Kutta scheme. The pressure Poisson equation at each fractional step is solved using pseudo-spectral approach with appropriate three-dimensional fast Fourier transforms. Adopting the concept of modified wavenumbers, the divergence-free condition is ensured up to machine accuracy. In addition, the body force involved in our forcing method is also implemented in every sub-timestep. See Laizet & Lamballais (2009), Laizet & Li (2011) for more details of the code and its validation, especially the treatment of the body force and pressure in spectral space. In the simulations, a constant flow rate is set and the bulk velocity U_b (flow rate divided by the channel cross-section area) is maintained at a constant value. All computations start with the same initial condition of a fully developed turbulent channel flow without control (the mean, root-mean-square velocity and Reynolds shear stress profiles were checked against the standard database to ensure the initial flow state). Table 1 shows the numerical details used for different cases in the present study. About 90 simulations were run with a control height $y_c^+ = 30$ at the friction Reynolds number around $Re_\tau (\equiv u_\tau h/\nu) = 180$, corresponding to the bulk Reynolds number $Re_b (\equiv u_b h/\nu) = 2800$. The computation domain is set to $4\pi \times 2 \times 2\pi/4\pi/6\pi$ and discretized on a Cartesian grid of $n_x \times n_y \times n_z = 192 \times 129 \times 128/256/384$. Here, different spanwise sizes of the box are used to accommodate different forcing spacings.

https://doi.org/10.1017/jfm.2018.553 Published online by Cambridge University Press

In addition, a few cases also explore how the drag reduction is sensitive to changes in y_c^+, which varied in the range 5–100. To examine the control method at moderate Re_τ, 45 simulations were also performed for different combinations of control parameters at $Re_\tau = 550$, corresponding to $Re_b = 10\,000$. The validation of the code, including the effects of the computational domain size and grid resolution, is provided in the Appendix.

We investigate how the forcing (2.3) changes the skin friction coefficient C_f, defined as

$$C_f = \frac{2\tau_w}{\rho U_b^2}, \tag{2.5}$$

where τ_w is the wall shear stress. The drag reduction $\mathcal{R}$ is quantified as the relative change in C_f:

$$\mathcal{R} = 1 - C_f/C_{f,0}, \tag{2.6}$$

where $C_{f,0}$ is the skin friction coefficient of the reference (uncontrolled) flow. Note that, C_f is evaluated by averaging over the entire channel wall area as well as over time after the initial transient when the flow adapts to the forcing and reaches the steady state; the averaging time (see table 1) is $900h/U_b$ and $600h/U_b$ for $Re_\tau = 180$ and 550, respectively. The transient time is estimated by direct observation of the time (T) history of the space-averaged skin friction, which is typically of the order of $100 \sim 300h/U_b$ as shown in Yao *et al.* (2017). For the drag reduction rate $\mathcal{R}$, its uncertainty $\delta\mathcal{R}$ is calculated by following the procedure in Gatti & Quadrio (2016), summarized as follows. First, the standard uncertainty σ_{C_f} of C_f is calculated via an autoregressive method as described by Oliver *et al.* (2014). Then the standard uncertainty $\sigma_\mathcal{R}$ of $\mathcal{R}$ is obtained by propagating the standard uncertainty of C_f for the uncontrolled and controlled cases (assuming they are independent variables (Gatti & Quadrio 2013)), i.e. $\sigma_\mathcal{R} = (C_f/C_{f,0})\sqrt{(\sigma_{C_f}/C_f)^2 + (\sigma_{C_{f,0}}/C_{f,0})^2}$. Finally, the uncertainty is extended to a 95 % confidence interval $\delta\mathcal{R} = z\sigma_\mathcal{R}$, here $z = 1.96$ is the standardized 95 % confidence interval of a normalized Gaussian probability density function. The uncertainty of $\mathcal{R}$ is reported in the text when applicable and plotted as error bar in the relevant figures.

3. Parametric study for $Re_\tau = 180$

Consideration is first given to the effects of different forcing spacings and amplitudes. Figure 2 shows the drag reduction $\mathcal{R}$ as a function of A^+ and λ^+ for $y_c^+ = 30$ (this choice of y_c^+ is discussed later) at $Re_\tau = 180$. The computations with forcing are carried out at seven different spacings λ^+ ranging from 45π to 1080π, corresponding to a simultaneous control of 1 to 35 low-speed streaks (noting that the mean spanwise spacing of the streaks $\lambda_z^+ \approx 100$ in the near-wall region (Kline *et al.* 1967; Smith & Metzler 1983)). Also, 13 different amplitudes in the range $0.003 \leqslant A^+ \leqslant 0.06$ are chosen. Thus, 91 total simulations are performed covering various A^+ and λ^+ values. The contours are computed from a linear interpolation of these discrete simulated points. It is rather impressive that $\mathcal{R}$ can be obtained in broad ranges of forcing amplitude and wavelength – a decidedly robust feature as precise selection and adherence to a particular value is not critical.

Figure 3(*a*) shows a non-monotonic variation of drag reduction $\mathcal{R}$ as a function of A^+ at $\lambda^+ = 360\pi$ and $y_c^+ = 30$. At small amplitudes, i.e. $A^+ < 0.006$, there is a slight drag increase, because the control flow is too weak to push streaks to merge,

https://doi.org/10.1017/jfm.2018.553 Published online by Cambridge University Press

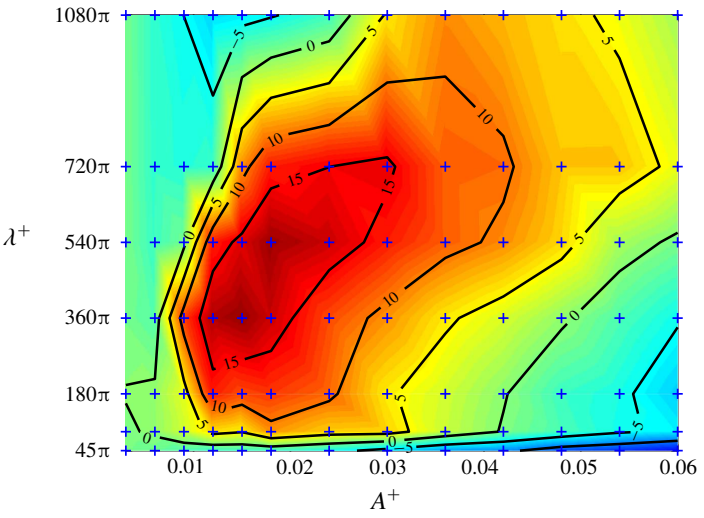


FIGURE 2. (Colour online) Drag reduction rate $\mathcal{R}$ (%) as a function of A^+ and λ^+ for $y_c^+ = 30$ at $Re_\tau = 180$. In this figure, the symbol + indicates the simulation data points used for interpolation.

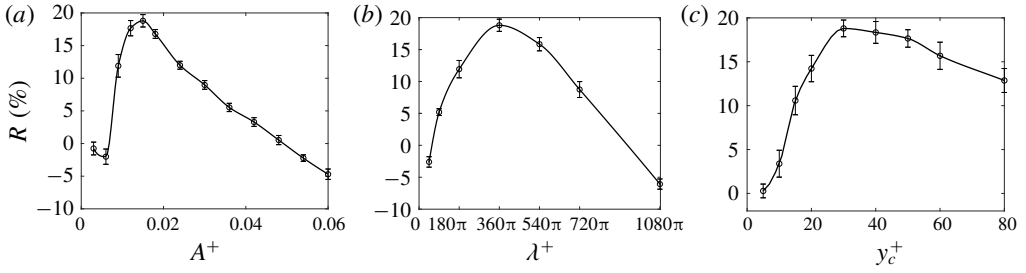


FIGURE 3. Drag reduction rate $\mathcal{R}$ (*a*) as a function of A^+ for $\lambda^+ = 360$ at $y_c^+ = 30$; (*b*) as a function of λ^+ for $A^+ = 0.015$ at $y_c^+ = 30$; (*c*) as a function of y_c^+ for $A^+ = 0.015$ and $\lambda^+ = 360\pi$. The error bar indicates the corresponding uncertainty of $\mathcal{R}$.

while additional Reynolds shear stresses are generated by the forcing, hence causing drag increase. As A^+ increases, suppression of Reynolds shear stress overcomes its enhancement due to merging of streaks, hence leading to drag reduction. The optimal $\mathcal{R}$ is $18.6\,\% \pm 0.9\,\%$ at $A^+ = 0.015$, and $\mathcal{R}$ deteriorates with increasing A^+. At $A^+ = 0.06$ (the largest forcing amplitude considered in this paper), $\mathcal{R}$ is actually increased by $4.1\,\% \pm 0.5\,\%$.

Similar trend is also found for λ^+. If λ^+ is too small (less than the spacing of two streaks), the control flow leads to no streak merging and hence no drag reduction. On the other hand, at much larger λ^+, the forcing is spread over in a larger spanwise domain, which is ineffective at causing the streaks to merge. Figure 3(*b*) shows $\mathcal{R}$ as a function of forcing spacing λ^+ at $A^+ = 0.015$ and $y_c^+ = 30$. Clearly, $\mathcal{R}$ increases with increasing λ^+ for $\lambda^+ \leqslant 360\pi$, but becomes less effective for $\lambda^+ > 360\pi$. The maximum $\mathcal{R}$ is approximately $18.6\,\% \pm 0.9\,\%$ and occurs at $\lambda^+ = 360\pi$, corresponding to a simultaneous control of approximately $10 - 15$ streaks by each swirl pair. Note the small drag increase (by $2.5\,\% \pm 0.8\,\%$) at $\lambda^+ = 45\pi$, where there is no merger of

https://doi.org/10.1017/jfm.2018.553 Published online by Cambridge University Press

streaks (since the control spacing $\lambda^+ \approx 140$ is close to the streak spacing) whilst the additional drag is caused by the Reynolds shear stress generated by the controlling swirls. Another feature of figure 3(*b*) is that there is a wide range of forcing spacing (i.e. $60\pi \lesssim \lambda^+ \lesssim 900\pi$) over which $\mathcal{R}$ is achieved.

Note that the optimal spacing $\lambda^+ = 360\pi$ in this paper is consistent with the optimal wavelength $\lambda^+ = 1200$ found by Canton *et al.* (2016*a*). Interestingly, $\lambda^+ = 360\pi$ also matches well with the optimal value of several other drag reduction techniques. For example, similar spanwise modulation scales are also found by Berger *et al.* (2000) in their Lorentz forcing control, Ricco & Hahn (2013) in their rotating disk wall control, Ghebali, Chernyshenko & Leschziner (2017) in their wavy wall configurations. However, the optimal spanwise spacing in some other strategies is quite different; for example, Segawa *et al.* (2007) obtain a maximum $\mathcal{R}$ of 5–7 % utilizing the alternating blowing and suction configurations whose spanwise spacing is only 300 (+ units). As for spanwise wall oscillation control, a characteristic spanwise displacement 1400 (+ unit) can be obtained based on the study of Jung *et al.* (1992) by converting their optimal oscillating period to the spanwise spacing. However, since the drag reduction increases with the maximum wall velocity (Quadrio & Ricco 2004; Yakeno *et al.* 2014), there seems to be no optimal spanwise wall displacement for the spanwise wall oscillation method. It would be interesting to compare these seemingly different control methods and to determine the underline physical mechanism for the selection of the optimal wavelength or oscillation period.

The effect of different control heights y_c^+ on drag reduction $\mathcal{R}$ is considered here. Note that a complete investigation of the effect of y_c^+ under the variation of other two controlling parameters is a computational challenge. Hence, for illustration, only the optimal spacing ($\lambda^+ = 360\pi$) and amplitude ($A^+ = 0.015$) identified above are considered here. In fact, we also find similar amounts of $\mathcal{R}$ when λ^+ and A^+ both increase, e.g. $\mathcal{R} = 18.3\,\% \pm 0.9\,\%$ can be achieved at $\lambda^+ = 540\pi$ and $A^+ = 0.018$. However, the smaller A^+ is obviously preferred as less energy input is required (discussed in § 5.1). Figure 3(*c*) shows $\mathcal{R}$ for different y_c^+ at $A^+ = 0.015$ and $\lambda^+ = 360\pi$, where the optimal y_c^+ is 30. For a smaller y_c^+ (say, $= 5$), $\mathcal{R}$ is only $1.4\,\% \pm 0.7\,\%$, because the wall jet is too thin to affect most parts of the streaks. For a much larger y_c^+ (say, $= 80$), $\mathcal{R}$ is $13.5 \pm 1.1\,\%$. Note that as y_c^+ increases, the downwash of the primary swirls, due to the constraint of the upper wall, becomes strong enough to increase drag, and the secondary swirls are also larger and stronger, so that their own high momentum downwash will increase the skin friction. These two effects combine together to decrease the effect of $\mathcal{R}$ imposed by the control flow and may even cause drag increase as y_c^+ increases. Thus, we conclude that a too large y_c^+ is to be avoided at high *Re*.

4. Analysis of drag reduction

To understand the mechanisms of both drag reduction and increase by the forcing, flow statistics as well as the dynamics are examined in detail below for the effects of A^+ and y_c^+ only. We focus only on these two parameters as we consider them to be the more important of the three, in order to limit the scope and size of the paper.

4.1. *Triple decomposition*

In view of the steady control flow, different from both the mean flow and turbulent fluctuations, it seems natural to interpret the total flow from the perspective of the

https://doi.org/10.1017/jfm.2018.553 Published online by Cambridge University Press

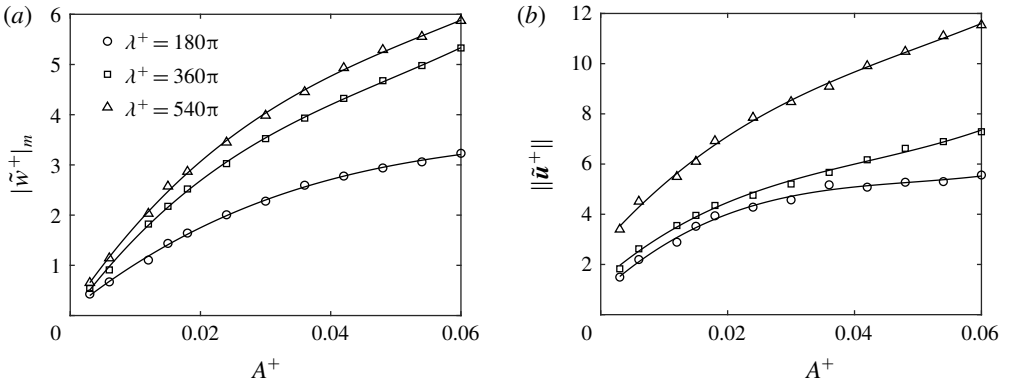


FIGURE 4. Forcing amplitude (A^+) dependence: (a) the maximum mean spanwise velocity $|\tilde{w}|_m$ and (b) $\|\tilde{\boldsymbol{u}}\|$ at $Re_\tau = 180$. Superscript $+$ indicates scaling with u_τ of uncontrolled flow. Different symbols represent different controlling wavenumbers λ^+.

following three components by using the triple decomposition (Reynolds & Hussain 1972):

$$\boldsymbol{u}(x, y, z, t) = \boldsymbol{U}(y) + \underbrace{\tilde{\boldsymbol{u}}(y, z) + \boldsymbol{u}''(x, y, z, t)}_{\boldsymbol{u}'}. \tag{4.1}$$

Here, $\boldsymbol{u}$ is the instantaneous total velocity field; $\boldsymbol{U} = \langle \overline{\boldsymbol{u}} \rangle$ is the mean velocity, where the overbar indicates averaging in time and in the streamwise direction – and also includes averaging in the spanwise direction if more than one spanwise wavelength is contained in the computational domain; and the bracket $\langle \cdot \rangle$ indicates spanwise averaging over one period; $\boldsymbol{u}' = \boldsymbol{u} - \boldsymbol{U}$ is the total fluctuation; $\tilde{\boldsymbol{u}} = \overline{\boldsymbol{u}} - \boldsymbol{U}$ is the so-called 'organized field' representing the coherent motion induced by the swirls; and $\boldsymbol{u}'' = \boldsymbol{u} - \overline{\boldsymbol{u}}$ is the random turbulent fluctuation.

Since the forcing amplitude A^+ does not correspond to a directly measurable quantity in the flow, two quantities, based on $\tilde{\boldsymbol{u}}$, are employed to characterize the flow response to the forcing. The first one is the maximum mean spanwise velocity $|\tilde{w}|_m = \max\{|\tilde{w}|\}$, which characterizes the strength of the spanwise wall-jet motion. The second one is chosen to be the norm of $\tilde{\boldsymbol{u}}$,

$$\|\tilde{\boldsymbol{u}}\| = \sqrt{\frac{1}{\Omega}\int_\Omega \tilde{\boldsymbol{u}} \cdot \tilde{\boldsymbol{u}}\, \mathrm{d}\Omega}, \tag{4.2}$$

where Ω is the total volume of the computational domain. $\|\tilde{\boldsymbol{u}}\|$ represents the volume-averaged kinetic energy of the induced motion. The variations of the two quantities as a function of the forcing amplitude are shown in figure 4 for three different λ^+ values. As expected, both $|\tilde{w}|_m$ and $\|\tilde{\boldsymbol{u}}\|$ increase with increasing A^+ and λ^+. In addition, we also find that, at a given A^+, the increase of $|\tilde{w}|_m$ with the increase of λ^+ becomes slower, in comparison to the faster increase of $\|\tilde{\boldsymbol{u}}\|$ with λ^+, which implies the ineffectiveness of a large forcing spacing, since more energy input is required to generate similar strengths of the spanwise wall-jet velocity as with small spacing. Interestingly, for high $\mathcal{R}$ cases, $|\tilde{w}|_m \approx 2 \sim 4u_{\tau,0}$, which is very close to the optimal spanwise perturbation velocity introduced by plasma actuators in TBL control (Thomas *et al.* 2016).

https://doi.org/10.1017/jfm.2018.553 Published online by Cambridge University Press

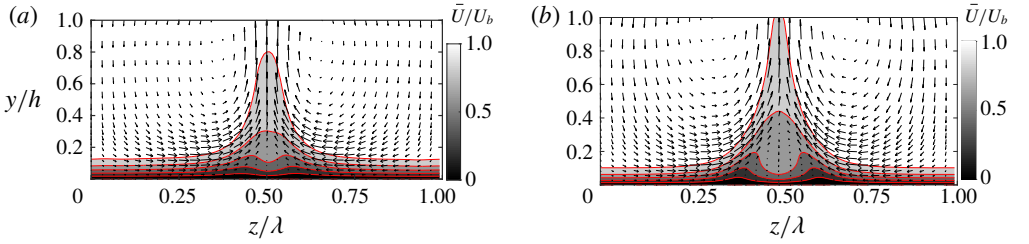


FIGURE 5. (Colour online) Cross-stream (y–z) plane view of mean velocity field ($\overline{\boldsymbol{u}}$) with the contours indicating the mean streamwise velocity (normalized by the bulk velocity U_b), and the vectors denoting the wall-normal and spanwise velocities for (*a*) $A^+ = 0.015$; (*b*) $A^+ = 0.06$ with $\lambda^+ = 360\pi$ and $y_c^+ = 30$.

Figure 5(*a*,*b*) shows the cross-streamwise view (y–z plane) of contours of the streamwise velocity and the cross-plane velocity vectors of $\overline{\boldsymbol{u}}$ at two different forcing amplitudes $A^+ = 0.015$ (corresponding to the optimal control case) and $A^+ = 0.06$ (corresponding to a drag increase case) with $\lambda^+ = 360\pi$ and $y_c^+ = 30$. For $A^+ = 0.015$, the topmost low-speed streak envelope, which has only one peak, is due to the lift-up effect of the counter-rotating control swirls, and extends up to the outer flow region ($y/h > 0.6$). Near the wall, however, the streak has dual peaks, which are due to the secondary swirls. As the forcing amplitude increases to $A^+ = 0.06$, the lift-up effect of the control swirls becomes even stronger; and the topmost low-speed streak extends up to the half-channel height. In addition, the near-wall streaks fall apart more due to the effect of stronger secondary swirls.

To compare the turbulent fluctuations with those in the uncontrolled case, figure 6 shows the spanwise-averaged velocity $\{\langle\overline{u_i''^2}\rangle^{1/2}\}^*$ and vorticity $\{\langle\overline{\omega_i''^2}\rangle^{1/2}\}^*$ fluctuations at two forcing magnitudes $A^+ = 0.015$ and 0.06 (the superscript $*$ indicates non-dimensionalization by the wall units of the controlled flow). All of the velocity and vorticity fluctuations are suppressed near the wall due to the merger of numerous streaks and hence fewer streamwise vortices are regenerated under control; however, they are all enhanced in the outer region ($y/h > 0.6$), mainly due to the advection of the large-scale control swirls, which transport the near-wall turbulence and vortical structures to the outer flow (see § 4.3). Notable differences are also observed by comparing $A^+ = 0.015$ and 0.06. In the outer region, all the turbulent fluctuations are further increased for the $A^+ = 0.06$ case, which is, as expected, due to the even stronger advection effect of the control swirls. In the near wall, the root mean square (r.m.s.) of v'', w'' and ω_x'' are increased, and u'', ω_y'' and ω_z'' are decreased, which is consistent with figure 13(*e*) where more streamwise aligned vortices are observed near the collision region of two swirls.

4.2. *Scales of drag production*

To analyse the contribution of the drag coefficient, the FIK (Fukagata, Iwamoto, Kasagi) identity (Fukagata *et al.* 2002; Rastegari & Akhavan 2015), which links the skin friction with the total Reynolds shear stress $\langle\overline{u'v'}\rangle$, is invoked:

$$C_f = \underbrace{\frac{12}{Re_b}}_{C_f^L} + \underbrace{12\int_0^2 (1-y)\left(-\frac{\langle\overline{u'v'}\rangle}{4U_b^2}\right)\mathrm{d}y}_{C_f^T}. \tag{4.3}$$

https://doi.org/10.1017/jfm.2018.553 Published online by Cambridge University Press

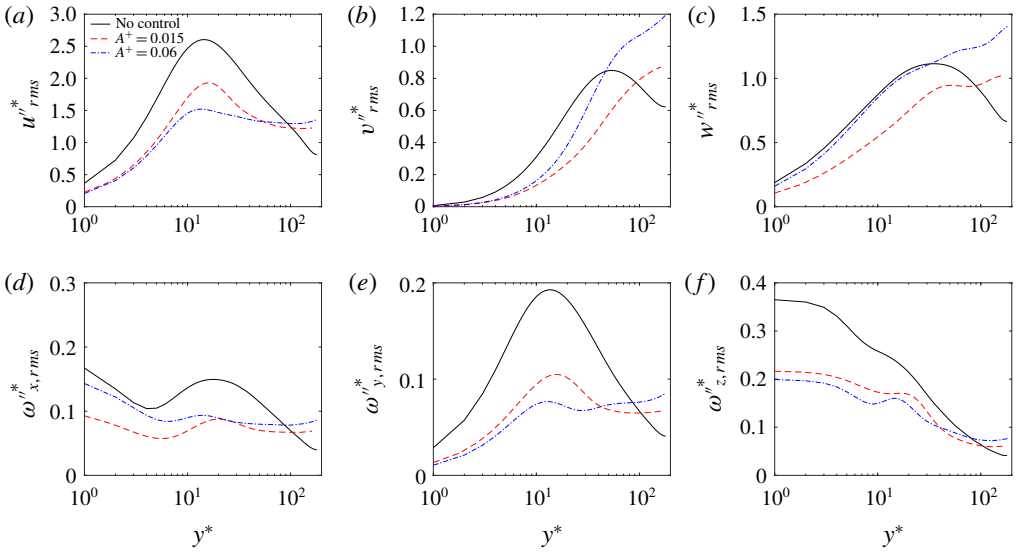


FIGURE 6. (Colour online) Spanwise-averaged turbulent velocity (top row) and vorticity (bottom row) fluctuations with various forcing amplitudes for $\lambda^+ = 360\pi$ and $y_c^+ = 30$. Solid line: uncontrolled case; dashed line: drag reduction with $A^+ = 0.015$; dash-dotted line: drag increase with $A^+ = 0.06$.

The drag coefficient C_f thus has an 'equivalent' laminar part $C_f^L = 12/Re_b$, and a turbulent part C_f^T represented by the weighted integration of the total Reynolds shear stress (RSS) $\langle\overline{u'v'}\rangle$. As the latter is composed of a coherent part $\langle\tilde{u}\tilde{v}\rangle$ and a random part $\langle\overline{u''v''}\rangle$, the FIK identity can be further decomposed as

$$C_f = \underbrace{\frac{12}{Re_b}}_{C_f^L} + \underbrace{12\int_0^2 (1-y)\left(-\frac{\langle\tilde{u}\tilde{v}\rangle}{4U_b^2}\right)\mathrm{d}y}_{C_f^C} + \underbrace{12\int_0^2 (1-y)\left(-\frac{\langle\overline{u''v''}\rangle}{4U_b^2}\right)\mathrm{d}y}_{C_f^R}. \tag{4.4}$$

Since Re_b is held constant in all simulations under different control parameters, only changes in the other two parts (coherent C_f^C and random C_f^R) affect the drag. Figure 7(*a*) shows the profiles of the total weighted Reynolds shear stress (WRSS) $-(1-y)\langle\overline{u'v'}\rangle$, and figure 7(*b*) shows the coherent part $-(1-y)\langle\tilde{u}\tilde{v}\rangle$ (denoted as C-WRSS) and the random part $-(1-y)\langle\overline{u''v''}\rangle$ (denoted as R-WRSS). For the low amplitude $A^+ = 0.015$ case, the drag reduction, following (4.3), is due to the alteration of the Reynolds shear stress throughout the whole range of y. Further, from figure 7(*b*), we find that the random turbulent Reynolds shear stress is significantly suppressed, and the coherent part contributes the most to the total Reynolds shear stress. In contrast, at a very high amplitude ($A^+ = 0.06$), the drag increment is due to the enhancement of the coherent Reynolds shear stress away from the wall ($y^+ > 20$). This also can be clearly shown through the decomposed total skin friction (normalized by the uncontrolled total skin friction) in figure 8(*a*). For the uncontrolled case (no coherent part), the laminar part contributes 25.0 % to the skin friction, and the turbulent part contributes 75.0 %. For $A^+ = 0.015$, the random part contribution

https://doi.org/10.1017/jfm.2018.553 Published online by Cambridge University Press

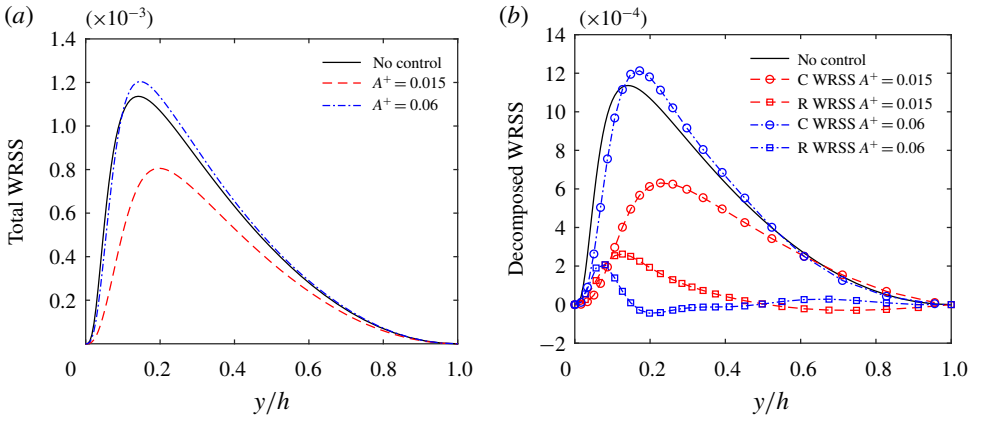


FIGURE 7. (Colour online) (*a*) Total and (*b*) decomposed weighted Reynolds shear stress (WRSS) distributions for different control amplitudes A^+ with $\lambda^+ = 360\pi$ and $y_c^+ = 30$ at $Re_\tau = 180$.

is reduced to 22.6 %, and the coherent part increased to 33.8 %; hence the net skin friction is reduced by 18.6 %. In contrast, for a higher $A^+ = 0.06$, although the random turbulent part is reduced to approximately 15.5 %, the coherent part is increased to 63.6 %, hence leading to the net skin friction increase of 4.1 %. (Note that figure 8(*b*) shows a similar analysis of C_f for the effect of different y_c^+, to be discussed in § 4.4.) Therefore, effective drag reduction results from a compensative effect of suppressing random turbulence (via suppression of the streaks as well as the streamwise vortices) countered by enhancing the coherent part induced by the energetic forcing.

To quantify the contributions to the skin friction from different scales, the FIK identity in combination with the spanwise wavenumber spectrum of the Reynolds shear stress is also employed (see also de Giovanetti, Hwang & Choi (2016)). (These contributions do not exist independently because different scales results from nonlinear interactions among them.) The total Reynolds shear stress can be expressed in terms of the one-dimensional spanwise Reynolds shear stress spectral density $\Phi^T(y; k_z)$, i.e.

$$-\langle\overline{u'v'}\rangle = \int_{-\infty}^{\infty} \Phi^T(y; k_z)\,\mathrm{d}k_z, \tag{4.5}$$

where $k_z (= 2\pi/\lambda_z)$ is the spanwise wavenumber. Then, the Reynolds shear stress contributed by the motions with spanwise size λ_z smaller than a given cutoff wavelength $\lambda_{z,c}$ is:

$$-\langle\overline{u'v'}\rangle_c(y; \lambda_{z,c}) = 2\int_{k_{z,c}}^{\infty} \Phi^T(y; k_z)\,\mathrm{d}k_z, \tag{4.6}$$

where the cutoff wavenumber is $k_{z,c} = 2\pi/\lambda_{z,c}$. The above spanwise spectrum analysis can be similarly applied to the coherent Reynolds shear stress $-\langle\tilde{u}\tilde{v}\rangle_c = 2\int_{k_{z,c}}^{\infty} \Phi^C(y; k_z)\,\mathrm{d}k_z$ and the random turbulent stress $-\langle\overline{u''v''}\rangle_c = 2\int_{k_{z,c}}^{\infty} \Phi^R(y; k_z)\,\mathrm{d}k_z$. Therefore, one obtains the skin friction coefficient generated by the motions

https://doi.org/10.1017/jfm.2018.553 Published online by Cambridge University Press

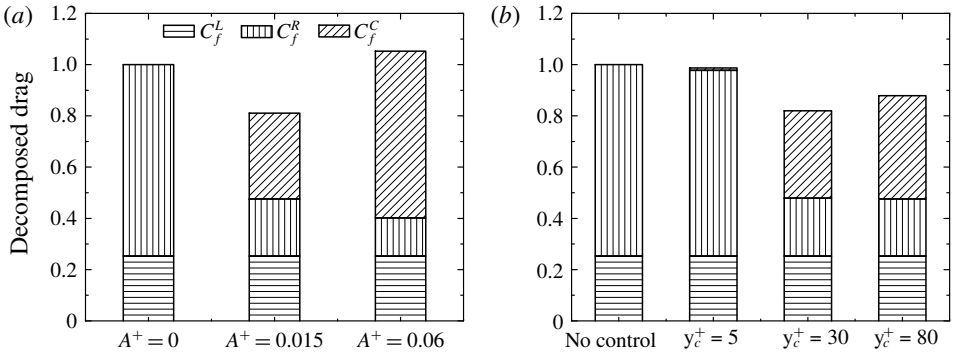


FIGURE 8. The decomposed drag (C_f^L, C_f^C, C_f^R) for (*a*) different A^+ and (*b*) different y_c^+ at $Re_\tau = 180$.

with $\lambda_z < \lambda_{z,c}$:

$$C_{f,c}(\lambda_{z,c}) = \frac{12}{Re_b} + \underbrace{12\int_0^2 (1-y)\left(-\frac{\langle \overline{u'v'}\rangle_c}{4U_b^2}\right)\mathrm{d}y}_{C_{f,c}^T}$$
$$= \frac{12}{Re_b} + \underbrace{12\int_0^2 (1-y)\left(-\frac{\langle \tilde{u}\tilde{v}\rangle_c}{4U_b^2}\right)\mathrm{d}y}_{C_{f,c}^C} + \underbrace{12\int_0^2 (1-y)\left(-\frac{\langle \overline{u''v''}\rangle_c}{4U_b^2}\right)\mathrm{d}y}_{C_{f,c}^R}, \tag{4.7}$$

which provides a tool to estimate the amount of drag contributed by coherent motions and random turbulent fluctuations of different scales.

The premultiplied spanwise wavenumber spectrum of the Reynolds shear stress $k_z\Phi^T$ for the uncontrolled case is displayed in figure 9(*a*). For $Re_\tau = 180$, it shows that the energy containing motions are mainly concentrated among $0.5 \lesssim \lambda/h \lesssim 1.1$ (or $100 \lesssim \lambda_z^+ \lesssim 200$) and $0.1 \lesssim y/h \lesssim 0.3$ (or $20 \lesssim y^+ \lesssim 50$) – these motions presumably correspond to quasi-streamwise vortices. This also explains the parametric study such that when setting y_c^+ within the buffer layer (figure 3*c*), the energy containing motions are effectively weakened and hence significant drag reductions can be achieved. The effects of control at $A^+ = 0.015$ on the spanwise wavenumber spectrum of the total ($k_z\Phi^T$) and coherent ($k_z\Phi^C$) Reynolds shear stresses are shown in figure 9(*b*,*c*), respectively. The difference of the two spectra represents the random turbulent contribution ($k_z\Phi^R$), which is induced mostly by the near-wall small-scale motions ($y < 0.3h$ and $\lambda_z < 2h$). It is obvious that the contribution to the total Reynolds stress is mainly due to the coherent motions, consistent with figure 8(*a*). Compared with the uncontrolled case, the contribution from the near-wall region is effectively suppressed; the energy containing part is shifted outward, while λ_z is also changed from $0.5h$ to approximately $3h$, the latter being close to the spacing of two adjacent control swirls. This suppression of structures at small scales is consistent with the observations of de Giovanetti, Sung & Hwang (2017) in their study of streak instability for large-scale motions. Note that, as the forcing amplitude increases to $A^+ = 0.06$, figure 9(*c*,*d*) shows that the Reynolds stress due to the coherent part (located in the outer region)

https://doi.org/10.1017/jfm.2018.553 Published online by Cambridge University Press

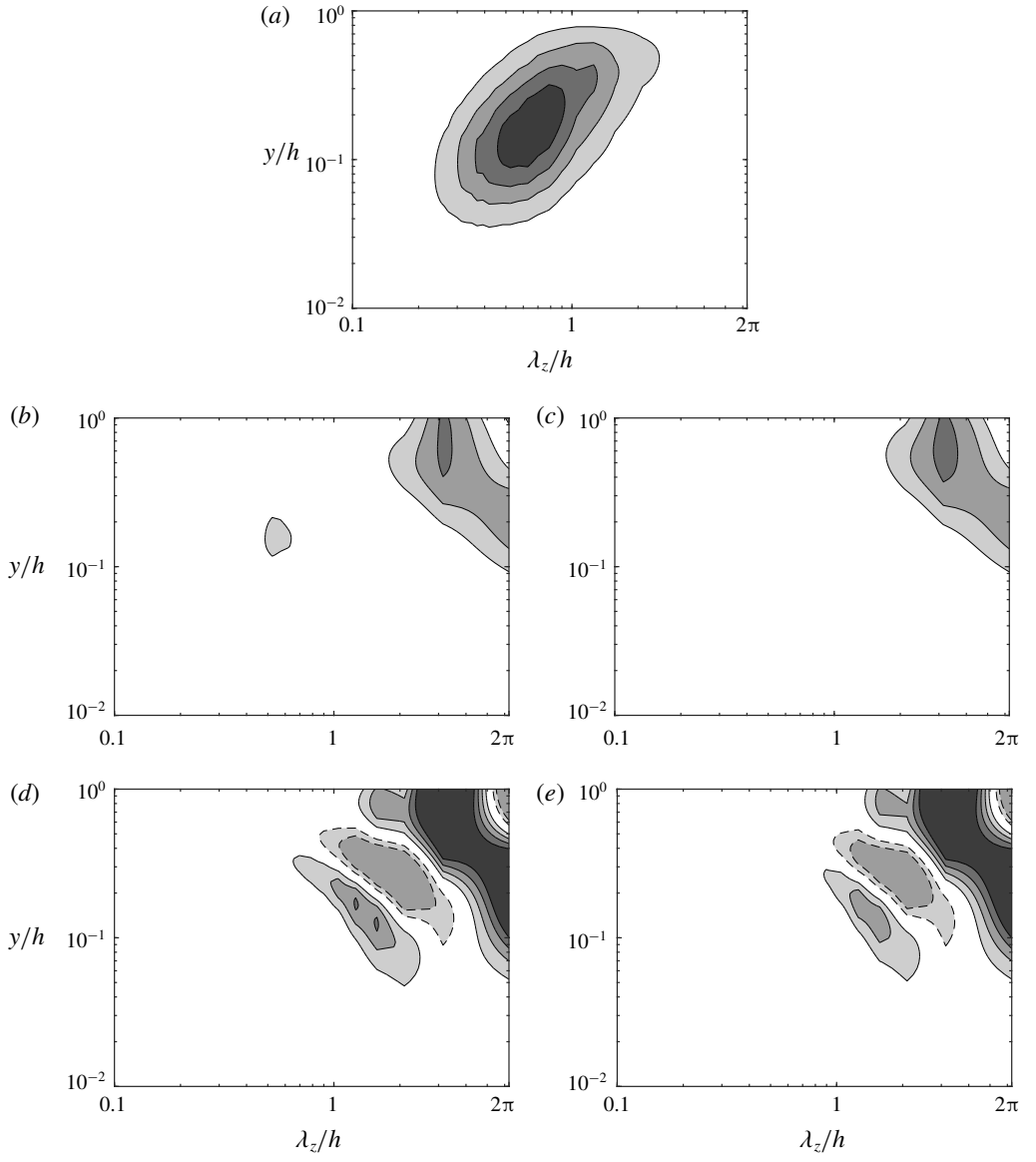


FIGURE 9. Premultiplied spanwise wavenumber spectra of the total Reynolds shear stress $k_z\Phi_{uv}^T$ for (*a*) uncontrolled flow; (*b*) $A^+ = 0.015$; and (*d*) $A^+ = 0.06$, and the coherent Reynolds shear stress $k_z\Phi_{uv}^C$ for (*c*) $A^+ = 0.015$, and (*e*) $A^+ = 0.06$. The contour labels indicate 0.2, 0.4, 0.6 and 0.8 of the maximum value of the uncontrolled case, and dashed lines for negative values.

further increases, while that from the random part is very small. Interestingly, there appears a positive Reynolds shear stress region (i.e. $1 < \lambda_z/h < 2$) marked by the dashed contours in figure 9(*d*,*e*), which actually results from the notable fluctuations in the Q1($u' > 0$, $v' > 0$) and Q3($u' < 0$, $v' < 0$) quadrants shown by the instantaneous velocity field in figure 11(*f*).

https://doi.org/10.1017/jfm.2018.553 Published online by Cambridge University Press

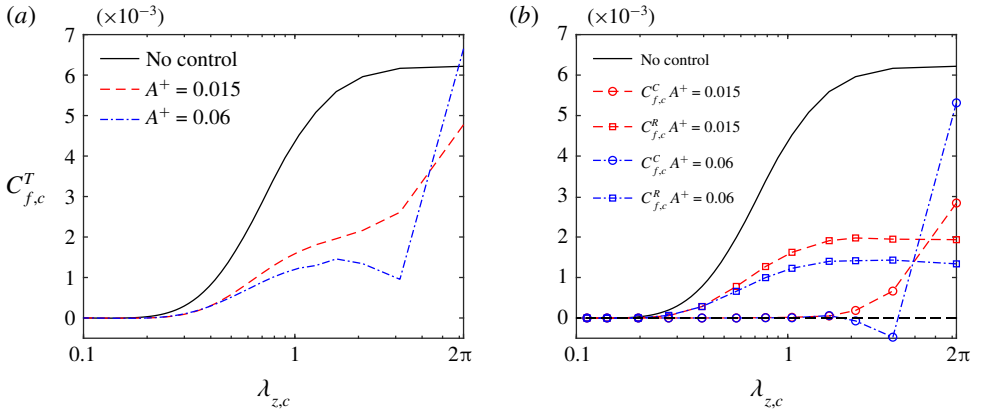


FIGURE 10. (Colour online) Cumulative friction coefficient of $C^T_{f,c}$ in (a), and of its coherent $C^C_{f,c}$ and random part $C^C_{f,c}$ in (b), varying with the cutoff spanwise wavelength $\lambda_{z,c}$. Note that the laminar part is subtracted from all of the plots.

Finally, figure 10 shows the cumulative skin friction due to the turbulent motions of $\lambda_z < \lambda_{z,c}$ for different A^+ values. The laminar part, identical for all cases, is subtracted from the plot so that all of the cumulative C_f values start from zero. For the uncontrolled case, motions with a spanwise scale in the range of $0.5h \leqslant \lambda_z \leqslant 1.5h$ are responsible for the majority of the drag (approximately 54 %), consistent with the observation by de Giovanetti *et al.* (2016). For controlled cases, the cumulative C_f contributed by the total Reynolds stress is plotted in figure 10(a), and that by the coherent and random Reynolds stresses are plotted in figure 10(b). Taking $A^+ = 0.015$ in figure 10(b) for example, the random Reynolds shear stress is mainly induced by small-scale motions ($\lambda_z < 2h$) and contributes to approximately 20 % of the total drag. In contrast, the coherent part is negligible for $\lambda_z < 2h$ and becomes important only when $\lambda_z > 2h$, beyond which the random part is almost unchanged, and the coherent part alone contributes to the total cumulative drag increase. In this case, the effect of suppressing the small scales exceeds that of enhancing the large scales, leading to net drag decrease. As A^+ increases to 0.06, the random turbulent part due to the small scales further decreases. Note particularly the dip of the coherent part near $\lambda_z \approx 2h$ is due the positive Reynolds shear stress identified in figure 9(e). Above this wavelength, the cumulative drag increases again due to the increasing contribution from the large-scale coherent motions. Thus, opposite to the $A^+ = 0.015$ case, the effect of excitation of the large scales at $A^+ = 0.06$ exceeds that of weakening the small-scale motions, hence leading to net drag increase.

4.3. *Coherent structures*

Figure 11 shows the contours of the low-speed streaks for both u' and u'' at $y^* = 20$ for different forcing amplitudes (uncontrolled $A^+ = 0$, low $A^+ = 0.015$ and high $A^+ = 0.06$). While typical meandering low-speed streaky structures are observed aligned along the streamwise direction in the uncontrolled case (figure 11a), the number of streaks is decreased for the controlled cases. In the presence of control, the basic near-wall streaks of u' are destroyed (figure 11b,d), and the near-wall flow becomes a single very wide meandering streak extending the entire flow length, as

https://doi.org/10.1017/jfm.2018.553 Published online by Cambridge University Press

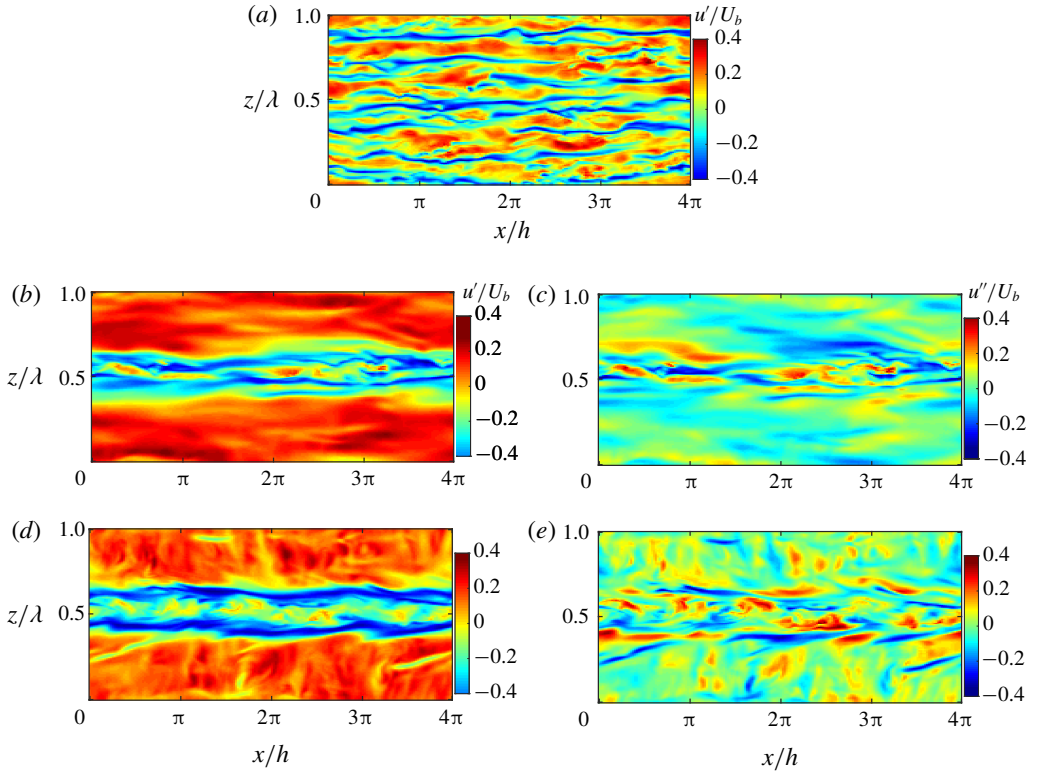


FIGURE 11. (Colour online) Contour of streamwise velocity fluctuations in the (x–z) plane at $y^* = 20$: (*a*) no control; (*b*) u' for $A^+ = 0.015$; (*c*) u'' for $A^+ = 0.015$; (*d*) u' for $A^+ = 0.06$; and (*e*) u'' for $A^+ = 0.06$. The forcing spacing is $\lambda^+ = 360\pi$ and control height is $y_c^+ = 30$.

expected from the merger of the numerous background streaks forced by the two wall jets. Note that such a widening and weakening of near-wall streaks has also been found in the drag reduction by spanwise wall oscillations (Jung *et al.* 1992; Akhavan, Jung & Mangiavacchi 1993), which presumably plays a similar role as SOJF merging many streaks together. The streaks are located essentially in the collision region – particularly clear in the random part u'' (figure 11*c*) when the coherent flow $\tilde{u}$ is subtracted from the total fluctuation velocity u'. As the forcing amplitude increases, more random streaks appear (figure 11*e*), which is consistent with the greater number of vortical structures observed in figure 13(*e*).

The flow field difference among the three different amplitudes is further examined through the velocity vectors in the cross-stream (y–z) plane, in figure 12. Here, the light (yellow) colour indicates positive streamwise velocity fluctuation u' and dark (blue) colour indicates negative streamwise velocity fluctuation u' (only the left half-domain $z/\lambda \leqslant 0.5$ is displayed, since the left and right parts are almost symmetric). Compared with the chaotic feature of the uncontrolled case (figure 12*a*), the velocity vectors near the wall are more parallel along the spanwise direction for $A^+ = 0.015$, indicating organized motions induced by SOJF similar to that of figure 5(*a*). Moreover, the downwash by the near-wall streamwise vortices observed in the uncontrolled case is significantly reduced by the SOJF. At higher $A^+ = 0.06$, the control flow is clearly

https://doi.org/10.1017/jfm.2018.553 Published online by Cambridge University Press

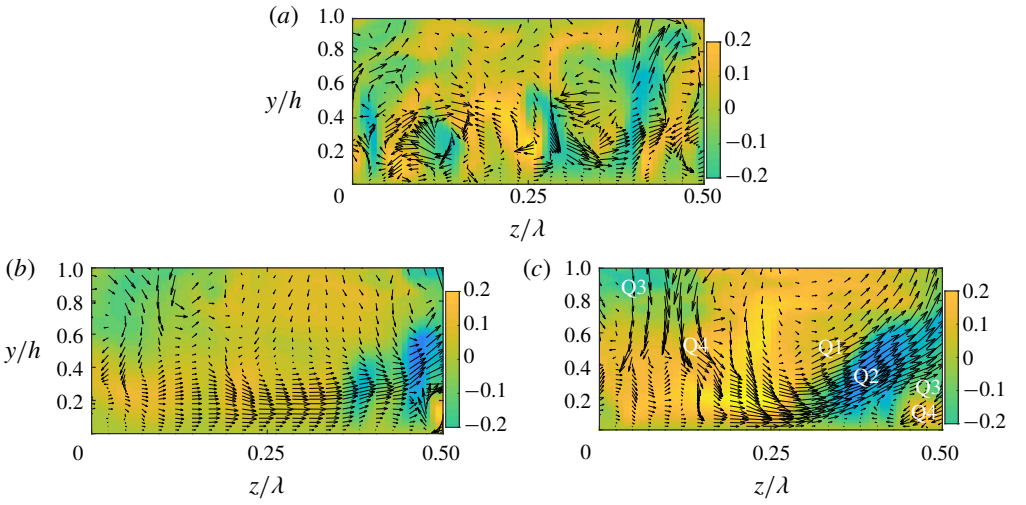


FIGURE 12. (Colour online) Vector plots of (v, w) in the $(y$–$z)$ plane located at $x = L_x/3$: (a) no control; (b) $A^+ = 0.015$; and (c) $A^+ = 0.06$. Light (yellow) and dark (blue) colours indicate positive and negative streamwise velocity fluctuations u'. The forcing spacing is $\lambda^+ = 360\pi$ and control height is $y_c^+ = 30$.

much more dominant and organized. As marked in figure 12(*c*), a strong Q2 event (negative u' and positive v' associated with the lift up of the large-scale swirls) occurs in the region $0.3 \lesssim z/\lambda \lesssim 0.5$, contributing to the increase of Reynolds shear stress in the bulk flow (figure 8) and hence drag increment. In addition, notable Q1 and Q3 events are also observed (located between Q2 and Q4 events), which cause the alternative positive/negative Reynolds shear stress contours in figures 9(*d*,*e*).

We then display the λ_2 vortices (Jeong & Hussain 1995) (calculated based on the random turbulent fluctuation velocity $\boldsymbol{u}''$) and the skin friction at the bottom wall in figure 13. Note that numerous slender vortices are distributed throughout the wall region in the uncontrolled case (figure 13*a*), lying directly above the high skin friction regions (figure 13*b*); and hairpins are few and far between, consistent with the observations of Schlatter *et al.* (2014). At $A^+ = 0.015$, most of the near-wall streamwise vortices disappear except near the collision region, just above the merged streak envelope (figure 13*c*); this disappearance is consistent with the suppression of $\omega''_{x,rms}$ in figure 6(*d*). From figure 13, we observe that the vortex structures mostly lie on top of the low skin friction region, which would appear to contradict the well-accepted notion that peak skin friction underlines streamwise vortices. This apparent enigma is reconciled below.

Figure 14 shows the instantaneous cross-section view of λ_2 contours at a specific streamwise location $x = L_x/3$, together with the associated low-speed streaks and the spanwise variation of wall shear stress. The strength of combined large streak envelope, although below the critical value, is so only on an average basis, some individual streaks survive on an instantaneous basis with very high flank angles (figure 14*c*,*d*). Although it may not be obvious, instantaneously the vortical structures, the streaks and wall shear stress are quite uniquely related; there are instances and locations of high instantaneous wall shear stresses, which can be uniquely identified with instantaneous streamwise vortical structures. However, after ensemble averaging,

https://doi.org/10.1017/jfm.2018.553 Published online by Cambridge University Press

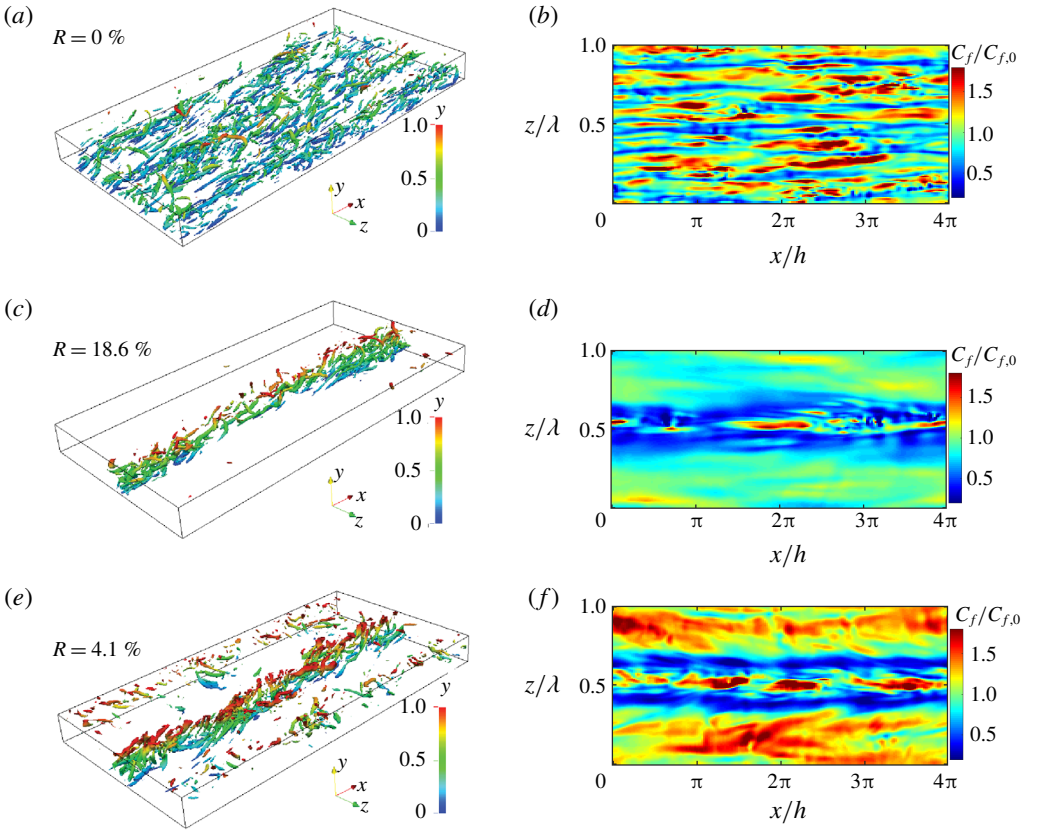


FIGURE 13. (Colour online) Iso-surfaces of $\lambda_2 = -1$ (shaded with the wall-normal distance from the bottom wall): (*a*) no control; (*c*) $\lambda^+ = 360\pi$ and $A^+ = 0.015$; (*e*) $\lambda^+ = 360\pi$ and $A^+ = 0.06$; (*b*,*d*) and (*f*) are the corresponding skin friction normalized by the uncontrolled case on the bottom wall.

the spiked wall shear stress is no longer apparent, due to the intermittent feature of these vortices.

The above investigation triggers another important question, i.e. where do these vortical structures above the streak envelope come from? Do they get pushed outward from the wall or freshly created locally? Note that since the vortices are predominantly streamwise (figure 13*c*), the evolutionary dynamics of ω_x is further investigated here. The inviscid evolution of ω_x is governed by

$$\frac{\partial \omega_x}{\partial t} = \underbrace{\omega_x \frac{\partial u}{\partial x}}_{\text{I}} - \underbrace{\frac{\partial w}{\partial x}\frac{\partial u}{\partial y}}_{\text{IIa}} + \underbrace{\frac{\partial v}{\partial x}\frac{\partial u}{\partial z}}_{\text{IIb}} - \underbrace{u\frac{\partial \omega_x}{\partial x}}_{\text{III}} - \underbrace{v\frac{\partial \omega_x}{\partial y} - w\frac{\partial \omega_x}{\partial z}}_{\text{IV}} + \underbrace{\frac{\partial F_z}{\partial y}}_{\text{V}}. \tag{4.8}$$

The terms on the right-hand side are: (I) vortex stretching, (IIa,b) vortex tilting, (III) streamwise advection, (IV) cross-stream advection and (V) vorticity generation due to forcing.

In order to get some clear understanding of the flow physics, it is necessary to evaluate the role of each term in the vorticity equation (4.8). Note that for

https://doi.org/10.1017/jfm.2018.553 Published online by Cambridge University Press

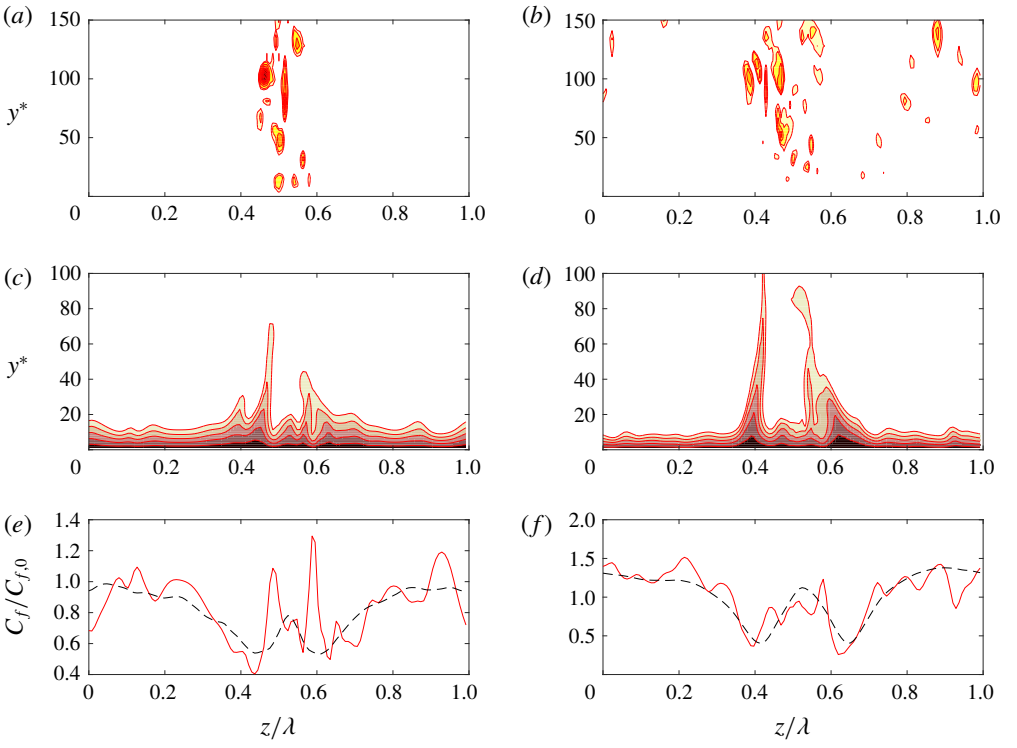


FIGURE 14. (Colour online) (*a*,*b*) Cross-section view of the instantaneous λ_2 structures; (*c*,*d*) low-speed streaks; and (*e*,*f*) spanwise distribution of the wall shear stress at streamwise location $x = L_x/3$. Note that the dashed line in the bottom row is the streamwise- and time-averaged wall shear stress. The left and right columns are for $A^+ = 0.015$; and $A^+ = 0.06$, respectively.

simplicity, we focus on the structures with positive streamwise vorticity $+\omega_x$ (SP) and their generation, ignoring the comparable numbers of negative streamwise vorticity $-\omega_x$ (SN) structures. Figure 15 shows a small domain around the mid-span of figure 14: (*a*) ω_x associated with SPs, along with the low-speed streak boundary from figure 14(*c*); (*b*) ω_x generation by the forcing term (V); (*c*) ω_x generation by wall-normal vorticity titling ($-\partial_x w \partial_y u$, IIa); (*d*) ω_x generation by spanwise vorticity titling ($\partial_x v \partial_z u$, IIb); (*e*) streamwise vortex stretching (I); and (*f*) cross-stream advection (IV). Note that the key $+\omega_x$ contours (SP structures) from figure 15(*a*) are repeated in figures 15(*b–f*) in order to provide a common spatial reference. Generation terms which strengthen SP are indicated by positive values (solid lines), while negative values indicate local weakening of SP (dash-dot lines).

At location *A* in figure 15(*b*), one SP is generated by the shearing induced by forcing. Most of the SPs are located in the middle region ($z/\lambda \sim 0.5$), where the forcing generation term is small. The source of generation of these SPs with $+\omega_x$ is mainly the tilting of spanwise and wall-normal vorticity by the streamwise flow induced shear. For example, in the near-wall region ($y^* < 50$, *B* in figure 15*c*), we find important vorticity generation due to the wall-normal vorticity tilting $-\partial_x w \partial_y u$ by the streamwise flow, where the instantaneous streak has a steep flank ω_y (figure 15*c*). In the bulk flow (at point *C* in figure 15*d* where $y^* \sim 50$), the spanwise vorticity

https://doi.org/10.1017/jfm.2018.553 Published online by Cambridge University Press

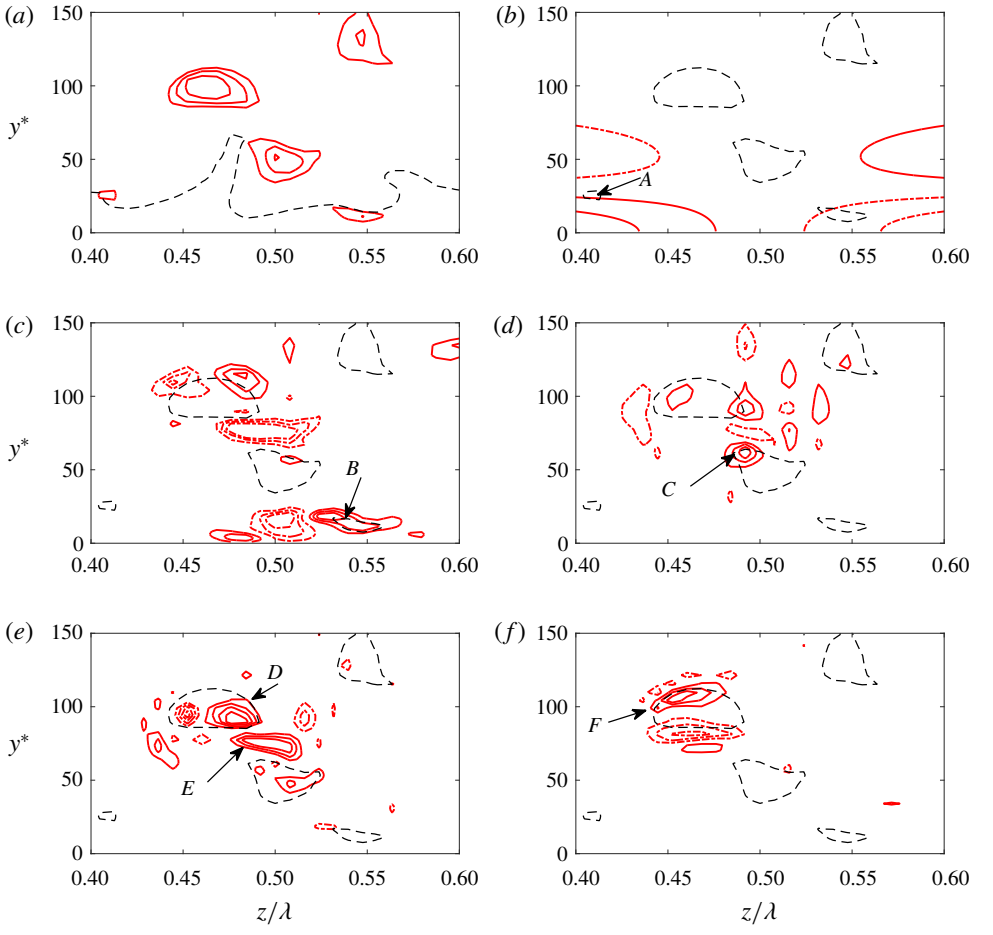


FIGURE 15. (Colour online) Contours (red lines) of (*a*) ω_x; (*b*) forcing generation; (*c*) the $-\partial_x w \partial_y u$ (wall-normal vorticity) tilting; (*d*) the $\partial_x v \partial_z u$ (spanwise vorticity) tilting; (*e*) vortex stretching; (*f*) the cross-stream (y–z) advection. The dash line in (*a*) indicates the low-speed streak in figure 14(*a*); (*b–f*) identify the positive ω_x boundaries as shown in (*a*). Also in (*a–f*), solid (dot-dashed) lines indicate positive (negative) magnitudes of each term.

tilting by streamwise velocity enhances the SP due to the presence of highly lifted-up low-speed streak (having strong $\partial_z u$). Note that once SPs are generated, they are further amplified by the direct stretching due to the streak waviness $\partial_x u$ (similar to that observed by SH1), evident from the strong regions of $+\omega_x \partial_x u$ embedded in SP (region *D* in figure 15*e*). Note that the intense vortex stretching (producing $+\omega_x$ at point *E* in figure 15*e*), does not result in SP, due to the simultaneous counter-effect of the tilting (producing $-\omega_x$) in figure 15(*c*). Finally, the generated SP structures are further transported outward by the swirls as also downstream by the base flow, evident from the positive amplitude of the advection term on top of the SP in *F* in figure 15(*f*).

For the higher forcing amplitude $A^+ = 0.06$ case, the skin friction near the wall-jet sides is significantly increased (figure 14*f*) due to the squashing of the wall jet, and hence increased $\partial u/\partial y$ (figure 11*f*). Although numerous streaks merge into a

https://doi.org/10.1017/jfm.2018.553 Published online by Cambridge University Press

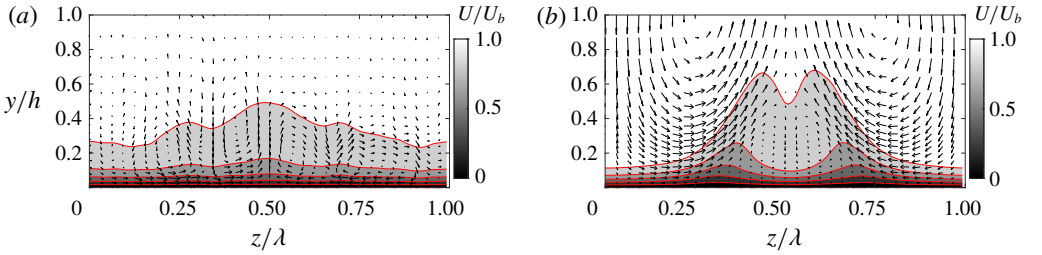


FIGURE 16. (Colour online) Cross-stream (y–z) plane view of (a) mean velocity field ($\overline{\boldsymbol{u}}$) with the contours indicating the mean streamwise velocity (normalized by U_b), and the vectors denoting the wall-normal and spanwise velocities for (a) $y_c^+ = 5$; (b) $y_c^+ = 80$.

large streak envelope, the streak strength is larger near the collision plane (figure 14d) compared with the small amplitude case $A^+ = 0.015$, and hence leads to the generation of more vortex structures, as seen in figure 14(b). In addition, the downwash of the secondary swirls is larger and stronger at high A^+ (i.e. $= 0.06$), which causes a local high skin friction at the mid-span (i.e. $z/\lambda \approx 0.5$ in figure 14f).

4.4. *The effect of* y_c^+

Compared with the previous large-scale control methods (Canton *et al.* 2016*a*, SH2), where the height of the control swirl was fixed at the centre of the channel, a major difference of the current SOJF method is the introduction of y_c to characterize the wall-jet height. To demonstrate the effect of y_c^+ on drag reduction $\mathcal{R}$, two additional cases with $y_c^+ = 5$ and 80 are discussed here (while $A^+ = 0.015$ and $\lambda^+ = 360\pi$ remain the same as the optimal for $y_c^+ = 30$). Compared with the case at $y_c^+ = 30$ (producing $18.6\,\% \pm 0.9\,\%$ of $\mathcal{R}$), $\mathcal{R}$ becomes $1.4\,\% \pm 0.7\,\%$ and $13.5\,\% \pm 1.1\,\%$ for $y_c^+ = 5$ and 80, respectively. Figure 16 shows the cross-streamwise view (the (y–z) plane) of contours of the streamwise velocity and the cross-plane velocity vectors of $\overline{\boldsymbol{u}}$ for the two different forcing height cases. For the low y_c^+ case, the wall jet is too thin, and limited very close to the bottom wall, which hardly has any effect on the suppression of the streaks, whilst at high y_c^+, the energetic, counter-rotating swirls well organize the flow, and the squashing effect along the sides of the swirls also becomes stronger. Compared to $y_c^+ = 30$, the secondary swirls at $y_c^+ = 80$ near the collision plane are much larger, separating the dual peaks further.

Figure 17 further shows the spanwise-averaged turbulent fluctuations $\{\langle\overline{u_i''^2}\rangle^{1/2}\}^*$. For $y_c^+ = 5$, turbulent fluctuations are almost unchanged, as extremely near-wall forcing is ineffective, as discussed above, also consistent with figure 8(b) where C_f^C is rather small and C_f^T is nearly unchanged. For $y_c^+ = 80$, the turbulent fluctuations are suppressed near the wall (due to the merger of streaks), while they are increased in the outer flow region (due to upward advecting of the structures). Since coherent motions are more pronounced at $y_c^+ = 80$ compared to $y_c^+ = 5$ (figure 16), a larger C_f^C is observed for $y_c^+ = 80$, as shown in figure 8(b). C_f^C is also 5 % larger at $y_c^+ = 80$ compared to that of $y_c^+ = 30$, leading to the degradation of $\mathcal{R}$ as y_c^+ increases.

Similar to figure 13, the λ_2 vortex and the corresponding skin friction at the bottom wall are displayed in figure 18 for $y_c^+ = 5$ and 80. It is obvious that the near-wall structures are barely suppressed at $y_c^+ = 5$ compared with the uncontrolled case. At $y_c^+ = 80$, much fewer vortex structures survive near the mid-span. In addition, there are

https://doi.org/10.1017/jfm.2018.553 Published online by Cambridge University Press

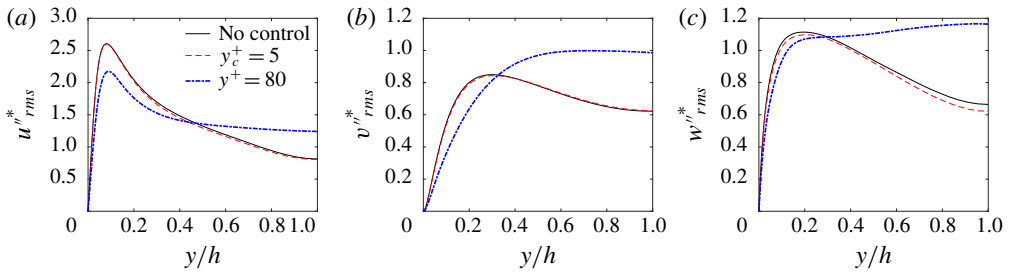


FIGURE 17. (Colour online) Spanwise-averaged turbulent velocity fluctuations for various forcing heights y_c^+ at $A^+ = 0.015$ and $\lambda^+ = 360\pi$.

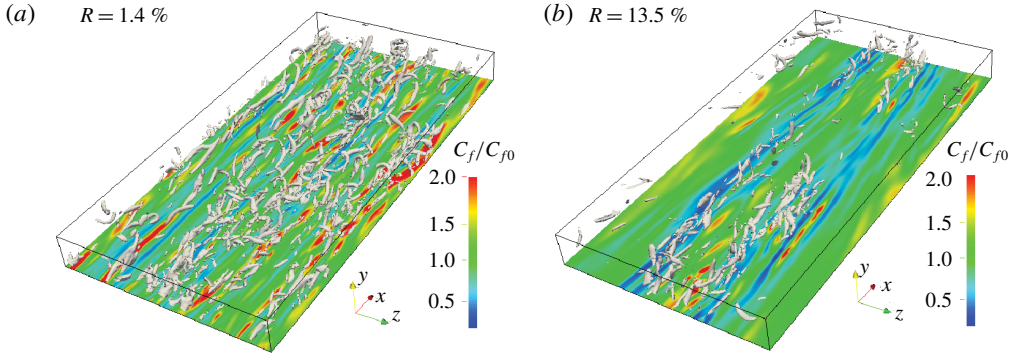


FIGURE 18. (Colour online) Iso-surfaces of $\lambda_2 = -1$ associated with the contours of the corresponding skin friction on the bottom walls normalized by the uncontrolled case: (*a*) $y_c^+ = 5$; (*b*) $y_c^+ = 80$ at $Re_\tau = 180$.

two distinct low skin friction regions lying along the streamwise direction, caused by the near-wall lifting up and separated by the larger secondary swirls. The downwash motions associated with the larger secondary swirls would cause drag increase and should be suppressed also. In summary, it is clear that y_c has to have an optimal value – neither too small nor too large.

5. Discussion

5.1. *Power performance*

Active control techniques are evaluated not only by $\mathcal{R}$, but also by the net power saving $\mathcal{N}$, subtracting the energy cost of the control. The value of $\mathcal{N}$, in a turbulent channel flow, is defined as

$$\mathcal{N} = \mathcal{R} - P_{in}/P_0, \tag{5.1}$$

where P_0 is the power required to drive the uncontrolled flow, and P_{in} is the control input power, calculated as $\int_\Omega \boldsymbol{f} \cdot \tilde{\boldsymbol{u}}\, \mathrm{d}\Omega$ by neglecting the electro-mechanical losses of a real actuator (Canton *et al.* 2016*b*; Mahfoze & Laizet 2017).

Figure 19(*a*,*b*) presents the energy input P_{in}/P_0 and the net power $\mathcal{N}$ as a function of A^+ and λ^+ at $y^+ = 30$. The energy input, quite small for small A^+, increases as A^+ and λ^+ increase. In particular, P_{in}/P_0 is only approximately 2.1 % for our optimal

https://doi.org/10.1017/jfm.2018.553 Published online by Cambridge University Press

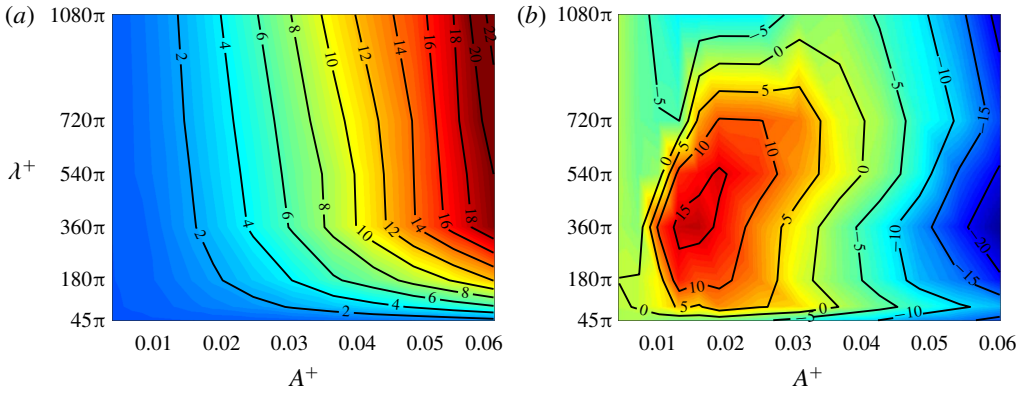


FIGURE 19. (Colour online) Map of (*a*) the power spent P_{in}/P_0 (%) and (*b*) net power saving $\mathcal{N}$ (%) as a function of A^+ and λ^+ for $y_c^+ = 30$ at $Re_\tau = 180$.

drag reduction case. From figure 19(*b*), it is obvious that the contour of net power saving is qualitatively similar to that of $\mathcal{R}$ shown in figure 2. It is encouraging to note that there is a wide range of control parameters yielding positive net power rates. The value of $\mathcal{N}$ for the optimal case ($A^+ = 0.015$ and $\lambda^+ = 360$) is approximately 16.5 %. Although this high net power saving is impressive, note that the value is based on a simple estimation of the actuation, where actuator's energy transfer efficiency has not been addressed. For real applications, it is known that currently many actuators suffer from a quite low energy transfer efficiency, i.e. around 1 % from electrical power to mechanical power for plasma-based actuators (Erfani *et al.* 2015; Mahfoze & Laizet 2017).

5.2. *Control efficacy at higher Re*

Another important issue for drag control methods is the performance at high *Re*. As shown in Yao *et al.* (2017), for given values of $y_c^+ = 30$, $\lambda^+ \approx 1200$ and $A^+ \approx 0.015$, $\mathcal{R}$ shows a gradual variation with *Re*-dependence. The degradation of $\mathcal{R}$ with increasing *Re* has also been observed in other control strategies, such as spanwise wall oscillations (Quadrio 2011; Gatti & Quadrio 2013, 2016) and the blow/suction method (Chung & Talha 2011). The reason seems to be the failure to control of the energetic large-scale structures at the high *Re* (de Giovanetti *et al.* 2016), which has also been explained in Gatti & Quadrio (2016) based on the upward shift of the viscous sublayer.

To better understand the *Re* dependence of our method, a limited parametric study is performed at $Re_\tau = 550$ (with y_c^+ range from 30, 50 to 70, λ^+ from $550\pi/3$ to 1100π and A^+ from 0.012 to 0.024). Figure 20(*a*) shows the drag reduction $\mathcal{R}$ as a function of A^+ and λ^+ at $y_c^+ = 30$. Compared with $Re_\tau = 180$ (figure 2), there is a moderate deterioration in $\mathcal{R}$. In particular, keeping the parameters same as found optimal at $Re_\tau = 180$, namely, $\lambda^+ \approx 1200$, $A^+ \approx 0.015$ and $y_c^+ = 30$ (denoted as case I), $\mathcal{R}$ decreases from $18.6\,\% \pm 0.9\,\%$ to $10.2\,\% \pm 0.8\,\%$ as Re_τ increases from 180 to 550 (note that a 2 % difference for $Re_\tau = 550$ reported in Yao *et al.* (2017) is due to a smaller box size used there). It does not necessarily imply that our method is less effective at high *Re*. Because of the strong dependence of $\mathcal{R}$ on the choice of forcing parameters, the drag reduction drop might be less pronounced in certain ranges of

https://doi.org/10.1017/jfm.2018.553 Published online by Cambridge University Press

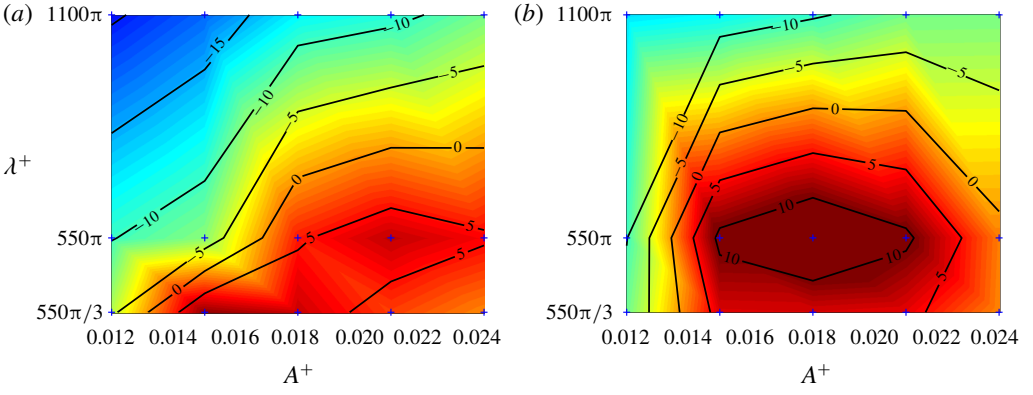


FIGURE 20. (Colour online) Drag reduction rate $\mathcal{R}$ (%) at $Re_\tau = 550$ as a function of A^+ and λ^+ for (*a*) $y_c^+ = 30$; (*b*) $y_c^+ = 50$.

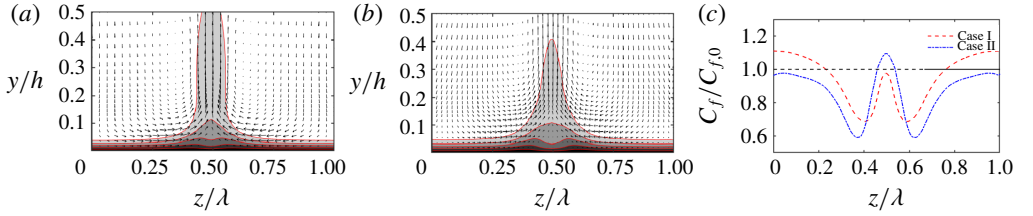


FIGURE 21. (Colour online) Cross-stream (y–z) plane view of (*a*) mean velocity field ($\overline{\boldsymbol{u}}$) for one control wavelength with the contours indicating the mean streamwise velocity (normalized by U_b), and the vectors denoting the wall-normal and spanwise velocities for (*a*) case I; (*b*) case II; (*c*) the associated spanwise distribution of the wall shear stress normalized with the uncontrolled case.

controlling parameters. For example, figure 20 shows that the forcing using $y_c^+ = 50$ is superior to that with $y_c^+ = 30$ – over a wide range with notable $\mathcal{R}$. A high $\mathcal{R}$ of $14.5\,\% \pm 0.8\,\%$ is achieved with slightly larger parameters $A^+ = 0.018$, $\lambda^+ = 1728$ and $y_c^+ = 50$ (denoted as case II). Different from previous near-wall drag control methods where the optimal parameters typically scale in wall units, the optimal control parameters of our large-scale SOJF method, to accommodate the outer shifted energy containing motions, seem to follow a mixed scaling. While y_c^+ increasing moderately with Re seems to follow the peak location of the Reynolds shear stress (see Xi, Hussain & She 2018), the control wavelength may scale in outer units – to be validated at higher Re simulations in the future.

To explain how this additional drag is achieved, flow field alterations by controls are examined. Figure 21 shows the cross-streamwise view of contours of the streamwise velocity and the cross-plane velocity vectors of $\overline{\boldsymbol{u}}$. Again, both cases clearly show the merged streak envelope, and the downwash motions between the large-scale swirls cause a dual peak of streak envelope near the wall, as well as a relatively high skin friction near the collision region compared to case I, which shows drag increase near the two sides of the swirls due to a small λ^+, case II produces smaller skin friction near the two sides, due to the smaller squashing effect observed in figure 21(*b*). Figure 22 shows the λ_2 structures and skin friction distribution at the bottom wall.

https://doi.org/10.1017/jfm.2018.553 Published online by Cambridge University Press

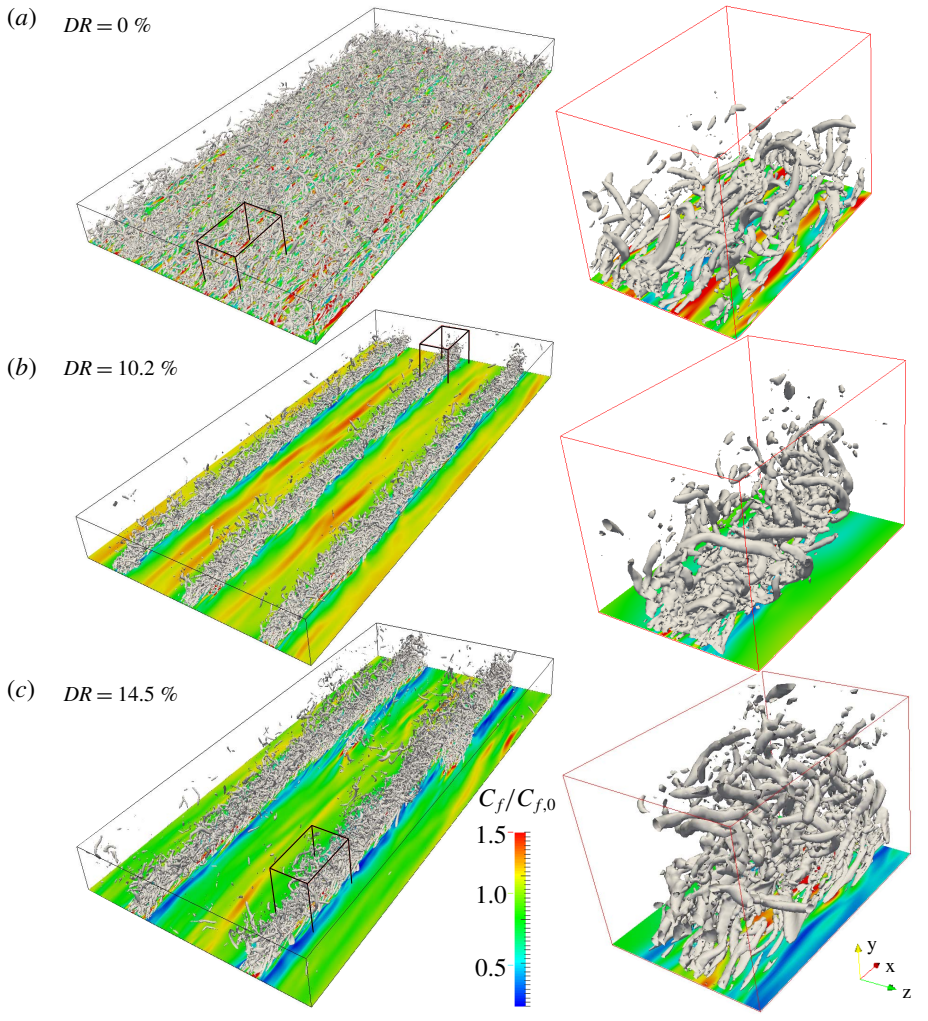


FIGURE 22. (Colour online) Iso-surfaces of $\lambda_2 = -1$ associated with the contours of the corresponding skin friction on the bottom walls normalized by the uncontrolled case: (*a*) uncontrolled; (*b*) case I; (*c*) case II. Note that the right column shows the zoomed views of the region marked on the left panel.

The vortical structures typically show a similar pattern as in the optimal case at $Re_\tau = 180$ (albeit the structures are far more numerous and packed in the high Re case): most of the vortices are eliminated except near the swirl collision region. Thus, it confirms that, at $Re_\tau = 550$, SOJF can successfully produce drag reduction through the merger of streaks, hence suppressing the vortical structures. Also note that a slight difference in vortex structure is observed for the two forcing cases when we look at the zoomed view: compared with case I, the vortical structures in case II are more aligned along wall-normal direction and extended up to the channel centre (due to a higher y_c^+ and A^+). Therefore, not surprisingly, different combinations of parameters can produces quite different vortical structure distributions and hence lead to different $\mathcal{R}$ values.

https://doi.org/10.1017/jfm.2018.553 Published online by Cambridge University Press

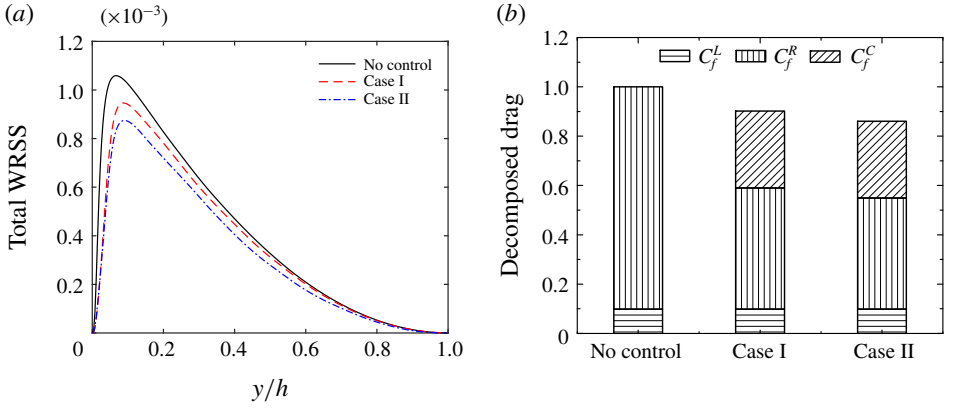


FIGURE 23. (Colour online) (*a*) Total weighted Reynolds shear stress (WRSS) distributions and (*b*) the decomposed drag (C_f^L, C_f^C, C_f^R) for different cases at $Re_\tau = 550$.

To better understand the flow physics altered by different combinations of controlling parameters, flow statistics are further examined. Figure 23(*a*,*b*) shows the profiles of the total weighted Reynolds shear stress and the decomposed total skin friction for different cases. Compared with the results at $Re_\tau = 180$, the degradation of $\mathcal{R}$ for case I is mainly due to less effective to suppress random turbulent fluctuations. In particular, while the coherent part contributes approximately 31.1 % to the skin friction, the random turbulent part is approximately 49.2 % for $Re_\tau = 550$ – in contrast to 22.6 % for $Re_\tau = 180$. Figure 24 further shows the premultiplied spanwise wavenumber spectra of the Reynolds shear stress ($k_z\Phi_{uv}$) for different controlled cases. The uncontrolled case at $Re_\tau = 550$ is displayed in figure 24(*a*,*b*) in outer and inner coordinates, respectively. Compared with the spectrum at $Re_\tau = 180$, the scale of the energy containing motions is increased at $Re_\tau = 550$ and spans from the inner scale ($\lambda_z^+ \approx 100$) to outer scale ($\lambda_z \approx 1.5h$). Also, these motions are concentrated in the buffer and log layers ($20 \lesssim y^+ \lesssim 300$), contributing most of the skin friction in uncontrolled flow. The spectrum for case I (figure 24*c*) shows that the energy containing motion at $\lambda_z^+ \sim 100$ ($\lambda_z/h \sim 0.2$) is significantly suppressed, hence leading to drag reduction. Also, due to the imposed large-scale swirls with wavelength $\lambda_z = 2\pi/3$, some specific modes with $\lambda_z = \pi/3$, $\pi/6$ are excited by the scale interaction (Duvvuri & McKeon 2015). A similar pattern of the spectrum is seen for the case II, expect with larger discrete scales of energy containing motions due to a larger $\lambda^+ = 1728$ (figure 24*d*).

Figure 25(*a*,*b*) shows the variation of cumulative C_f values, and their coherent and random parts, respectively. Compared with the uncontrolled flow, the total cumulative C_f is decreased for both cases. Similar to other control methods, the degradation of $\mathcal{R}$ with wall unit scaled parameters at $Re_\tau = 550$ is mainly due to the decrease of suppressing random turbulent fluctuations associated with large-scale motions (i.e. large λ_z). Moreover, compared to case I, the additional 4.3 % drag reduction for case II mainly results from a larger suppression of the random turbulent fluctuation in the range $0.5 \lesssim \lambda_z/h \lesssim 2$. As shown in figure 24(*a*,*b*), the energy containing motions' scale is increased and shifted away from the wall at $Re_\tau = 550$. Therefore, to suppress these motions to obtain effective drag reduction, the imposed control swirls should also feature a larger λ^+ and a higher y_c^+ compared to those at $Re_\tau = 180$. That is why case II yields more drag reduction than case I.

https://doi.org/10.1017/jfm.2018.553 Published online by Cambridge University Press

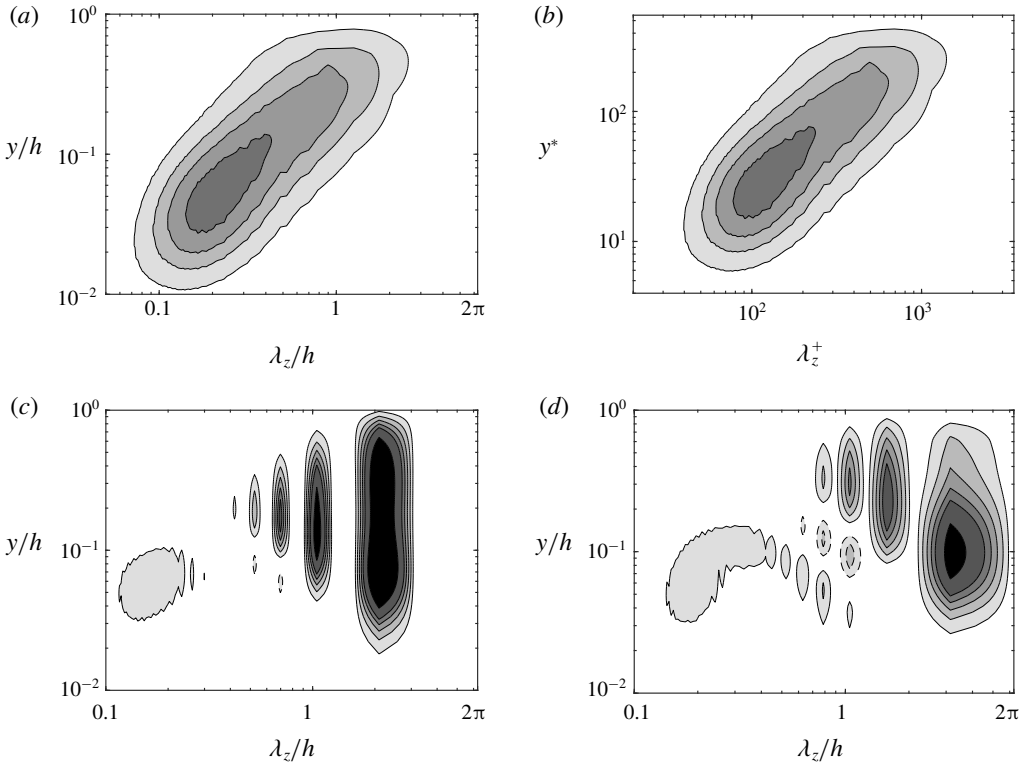


FIGURE 24. Premultiplied spanwise wavenumber spectra of the Reynolds shear stress at $Re_\tau = 550$ for (*a*) uncontrolled flow in outer unit; (*b*) uncontrolled flow in inner unit; (*c*) case I: $y_c^+ = 30$, $\lambda^+ = 1200$, $A^+ = 0.015$; (*d*) case II: $y_c^+ = 50$, $\lambda^+ = 1700$, $A^+ = 0.018$. The contour labels indicate 0.2, 0.4, 0.6 and 0.8 of the maximum value of the uncontrolled case, and dashed lines for negative values.

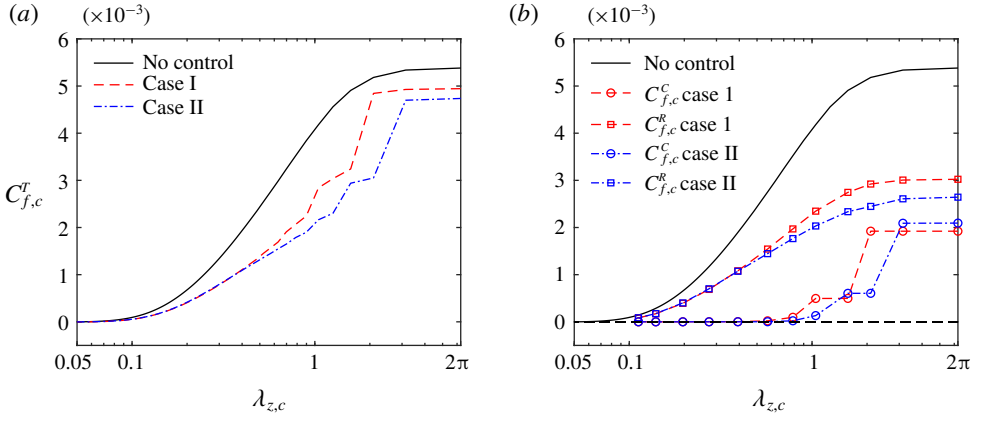


FIGURE 25. (Colour online) Variation of (*a*) $C_{f,c}^T$ and (*b*) its coherent $C_{f,c}^C$ and random part $C_{f,c}^R$ with the cutoff spanwise wavelength $\lambda_{z,c}$ at $Re_\tau = 550$.

https://doi.org/10.1017/jfm.2018.553 Published online by Cambridge University Press

It is possible that even higher drag reduction $\mathcal{R}$ may be achieved at $Re_\tau = 550$ by finer searching in a larger control parameter space; however, due to limited computation resources, this has not been pursued. Still, the above preliminary result showing $\mathcal{R} = 14.5\,\%$ is indeed encouraging, because it suggests the highly desirable prospect for significant $\mathcal{R}$ at even higher Re via simultaneously controlling even more streaks by each SOJF pair targeting at proper height. As Re increases, the role of outer structures becomes more important due to their larger contribution to skin friction. Therefore, controlling these outer structures might be necessary at high Re. On the other hand, caution should be given to controlling of large-scale motions (LSM) or very large-scale motions (VLSM), since recent studies show that suppression of LSM and VLSM does not yield significant drag reduction, as smaller scales may also be concomitantly altered due to nonlinear scale interaction (de Giovanetti *et al.* 2016; Abbassi *et al.* 2017). Note that larger control spacing and height of SOJF will require additional power input, which is indeed of concern for all control methods. For example, compared with 2.4 % for case I, P_{in}/P_0 increases to approximately 4.7 % for the controlling parameters employed in case II. These issues may limit the efficacy of our method at high Re, but important drag reduction might still be possible by optimizing the values of the controlling parameters. All these need further studies.

6. Conclusion

We performed a detailed study of drag control using SOJF in turbulent channel flows. A parametric search shows a maximum $\mathcal{R}$ of $18.6\,\% \pm 0.9\,\%$ at $Re_\tau = 180$ with $A^+ \approx 0.015$, $\lambda^+ \approx 1200$ and $y_c^+ \approx 30$. We find that by merging of many low-speed streaks together, the streak envelope slope and hence the average streak strength is weakened and the generation of streamwise vortices is substantially suppressed by the concomitant decreased instability/transient growth. However, as the forcing amplitude A^+ increases, the increased downwash near the swirl sides causes strong wall shear stress and hence leads to drag increment at very large A^+. The increased downwash is also observed, as expected, for larger y_c^+ cases, which also explains why the large scale control strategies become less effective at high Re when channel half-height is chosen as the swirl centre (Canton *et al.* 2016*b*).

Surprisingly, intense streamwise vortical structures are found to lie above the low average friction region in the control flow. Such location is due to the fact that the strength of combined large streak envelope, although definitely below the critical value, is so only on an average basis, while some individual streaks around the envelope centre survive on an instantaneous basis, whose flank angle values are still high, hence undergo instability/transient growth to continue generating streamwise vortices. The streamwise vorticity equation is also examined; the vortex tilting and stretching terms are found to play an important role in generating streamwise vortices in the mid-span of the channel, which then lead to instantaneous local high wall shear stress. However, after ensemble averaging, the spiked wall shear stress is no longer apparent.

By using the FIK identity in combination with the triple decomposition, we find that drag reduction primarily results from a compensative effect of suppressing random turbulence countered by enhancing the swirl induced coherent motions. At the optimal control condition, the random fluctuation, whose scale is smaller than that of the swirl, are significantly suppressed. When accounting for the energy cost of the control, net power saving of approximately 16.5 % can be achieved at the optimal case by neglecting the electro-mechanical losses.

https://doi.org/10.1017/jfm.2018.553 Published online by Cambridge University Press

Re_τ	$L_x/h, L_z/h$	$N_x \times N_y \times N_z$	Δx^+	$\Delta y_w^+, \Delta y_c^+$	Δz^+	$C_{f,0} \times 10^3$	$C_{f,opt} \times 10^3$	$\mathcal{R}$ (%)
180	$4\pi, 2\pi$	$192 \times 129 \times 128$	11.8	(0.91, 7.8)	8.8	8.25	6.72	18.6
	$8\pi, 6\pi$	$384 \times 193 \times 512$	11.8	(0.67, 5.4)	6.7	8.15	6.63	18.4
550	$4\pi, 2\pi$	$512 \times 193 \times 384$	13.4	(1.01, 11.4)	8.8	5.84	4.99	14.5
	$8\pi, 3\pi$	$1024 \times 385 \times 768$	13.4	(0.78, 8.7)	6.6	5.89	5.07	13.9

TABLE 2. Detailed parameters used for the resolution study. Here $C_{f,0}$ and $C_{f,opt}$ are the skin friction for the uncontrolled and optimal controlled cases, and $\mathcal{R}$ is the amount of drag reduction for the optimal case.

The control strategy is also applied at a higher $Re_\tau (= 550)$. Different from near-wall control strategies where the optimal parameters scale in wall units, the optimal parameters for SOJF seem to follow a mixed scaling. Compared with $10.2\,\% \pm 0.8\,\%$ drag reduction for wall scaled control parameters, $\mathcal{R} = 14.5\,\% \pm 0.8\,\%$ is obtained by slightly increasing the forcing spacing and height to accommodate the outer shifted energy containing motions. The possibility and limitations of applying our large-scale control strategy for even higher *Re* are discussed. Future study includes: (i) developing a model to link $\mathcal{R}$ and related factors induced by the forcing; and (ii) the exploration of applying the SOJF strategy to flat plate TBLs.

Acknowledgements

We thank E. Stout for his discussions, critical comments and a review of this manuscript. Computational resources were provided by Texas Tech University High Performance Computing Center (HPCC), and the Extreme Science and Engineering Discovery Environment (XSEDE) under grant no. TG-CTS180032.

Appendix. Adequacy of computational resolution and domain size

To save computational cost, the numerical resolution employed in the current study is marginal, especially at $Re_\tau = 550$. In addition, the size of our computational domain is of the same order as the largest scale generated by the forcing. It is natural to ask about the adequacy of the numerical resolution and computational domain size used in our study; to address both these issues, two additional simulations of larger computational domain size and finer grid resolution are performed at each Re_τ for both uncontrolled and optimally controlled cases. The details of domain sizes, grid sizes and resolutions used are listed in table 2. Figure 26 shows the mean velocity and the r.m.s. velocity fluctuations for the uncontrolled case. Our aforementioned results using the marginal simulation parameters exhibit good agreements with these additional studies with larger domain size and finer resolution; they both also agree with the direct numerical simulation (DNS) data of Lee & Moser (2015). Moreover, other flow quantities, e.g. wall shear stress, Reynolds shear stress, show little difference between different cases. Quantitatively, in particular, at each Re_τ value, the difference of the skin friction coefficient is less than 2 % between different domain sizes and resolutions for both uncontrolled and controlled cases. Since the deviations related to the domain size and resolution are of the same sign, the effect on $\mathcal{R}$ is found to be smaller: $\Delta\mathcal{R} < 1\,\%$.

https://doi.org/10.1017/jfm.2018.553 Published online by Cambridge University Press

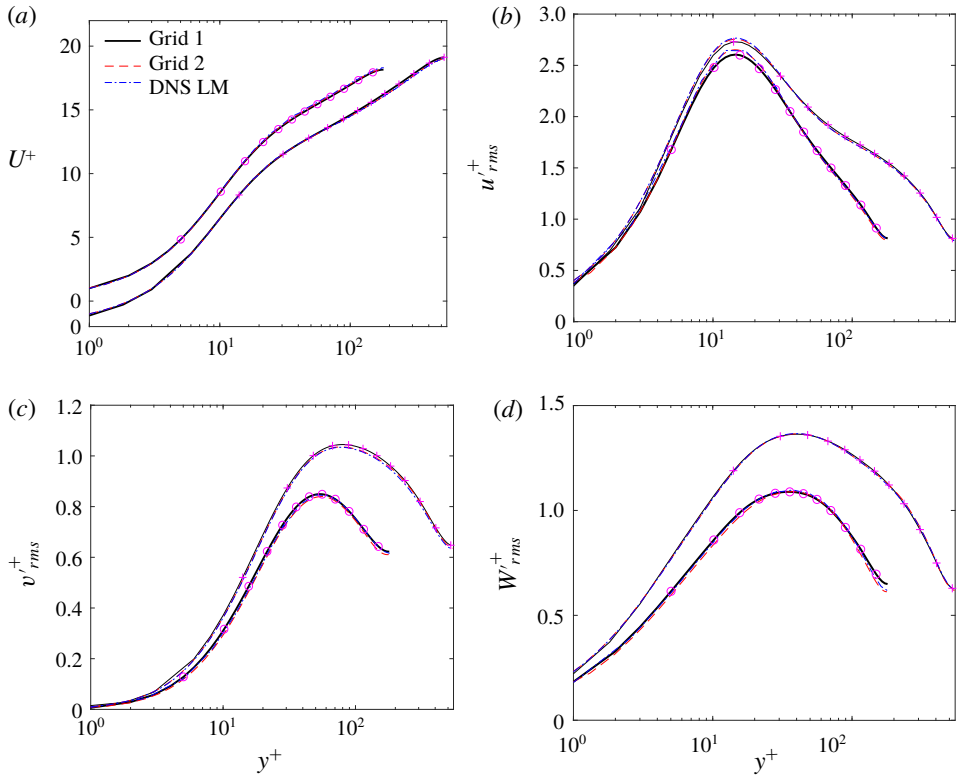


FIGURE 26. (Colour online) Comparison of profiles of: (*a*) mean velocity (U); (*b*) u'_{rms}; (*c*) v'_{rms}; and (*d*) w'_{rms} for the uncontrolled case at $Re_\tau = 180$ (○) and $Re_\tau = 550$ (+). Solid line: small domain; dash: large domain; and dash-dotted: DNS data from Lee & Moser (2015). In (*a*) the two profiles are vertically staggered for clarity.

REFERENCES

ABBASSI, M. R., BAARS, W. J., HUTCHINS, N. & MARUSIC, I. 2017 Skin-friction drag reduction in a high-Reynolds-number turbulent boundary layer via real-time control of large-scale structures. *Intl J. Heat Fluid Flow* **67**, 30–41.

AGOSTINI, L., TOUBER, E. & LESCHZINER, M. A. 2014 Spanwise oscillatory wall motion in channel flow: drag-reduction mechanisms inferred from dns-predicted phase-wise property variations at ret = 1000. *J. Fluid Mech.* **743**, 606–635.

AKHAVAN, R., JUNG, W. J. & MANGIAVACCHI, N. 1993 Turbulence control in wall-bounded flows by spanwise oscillations. In *Advances in Turbulence IV*, pp. 299–303. Springer.

BECHERT, D. W., BRUSE, M., HAGE, W., VAN DER HOEVEN, J. G. T. & HOPPE, G. 1997 Experiments on drag-reducing surfaces and their optimization with an adjustable geometry. *J. Fluid Mech.* **338**, 59–87.

BERGER, T. W., KIM, J., LEE, C. & LIM, J. 2000 Turbulent boundary layer control utilizing the lorentz force. *Phys. Fluids* **12** (3), 631–649.

BUTLER, K. M. & FARRELL, B. F. 1993 Optimal perturbations and streak spacing in wall-bounded turbulent shear flow. *Phys. Fluids* A **5** (3), 774–777.

CANTON, J., ÖRLÜ, R., CHIN, C., HUTCHINS, N., MONTY, J. & SCHLATTER, P. 2016*a* On large-scale friction control in turbulent wall flow in low Reynolds number channels. *Flow Turbul. Combust.* **97**, 1–17.

https://doi.org/10.1017/jfm.2018.553 Published online by Cambridge University Press

CANTON, J., ÖRLÜ, R., CHIN, C. & SCHLATTER, P. 2016*b* Reynolds number dependence of large-scale friction control in turbulent channel flow. *Phys. Rev. Fluids* **1** (8), 081501.

CHECCO, A., OCKO, B. M., RAHMAN, A., BLACK, C. T., TASINKEVYCH, M., GIACOMELLO, A. & DIETRICH, S. 2014 Collapse and reversibility of the superhydrophobic state on nanotextured surfaces. *Phys. Rev. Lett.* **112** (21), 216101.

CHOI, H., MOIN, P. & KIM, J. 1994 Active turbulence control for drag reduction in wall-bounded flows. *J. Fluid Mech.* **262**, 75–110.

CHOI, J.-I., XU, C.-X. & SUNG, H. J. 2002 Drag reduction by spanwise wall oscillation in wall-bounded turbulent flows. *AIAA J.* **40** (5), 842–850.

CHUNG, Y. M. & TALHA, T. 2011 Effectiveness of active flow control for turbulent skin friction drag reduction. *Phys. Fluids* **23** (2), 025102.

CORKE, T. C., ENLOE, C. L. & WILKINSON, S. P. 2010 Dielectric barrier discharge plasma actuators for flow control. *Annu. Rev. Fluid Mech.* **42**, 505–529.

DENG, B.-Q. & XU, C.-X. 2012 Influence of active control on stg-based generation of streamwise vortices in near-wall turbulence. *J. Fluid Mech.* **710**, 234–259.

DUVVURI, S. & MCKEON, B. J. 2015 Triadic scale interactions in a turbulent boundary layer. *J. Fluid Mech.* **767**, R4.

ERFANI, R., ZARE-BEHTASH, H., HALE, C. & KONTIS, K. 2015 Development of dbd plasma actuators: the double encapsulated electrode. *Acta Astron.* **109**, 132–143.

FUKAGATA, K., IWAMOTO, K. & KASAGI, N. 2002 Contribution of Reynolds stress distribution to the skin friction in wall-bounded flows. *Phys. Fluids* **14** (11), L73–L76.

GATTI, D. & QUADRIO, M. 2013 Performance losses of drag-reducing spanwise forcing at moderate values of the Reynolds number. *Phys. Fluids* **25** (12), 125109.

GATTI, D. & QUADRIO, M. 2016 Reynolds-number dependence of turbulent skin-friction drag reduction induced by spanwise forcing. *J. Fluid Mech.* **802**, 553–582.

GHEBALI, S., CHERNYSHENKO, S. I. & LESCHZINER, M. A. 2017 Can large-scale oblique undulations on a solid wall reduce the turbulent drag? *Phys. Fluids* **29** (10), 105102.

DE GIOVANETTI, M., HWANG, Y. & CHOI, H. 2016 Skin-friction generation by attached eddies in turbulent channel flow. *J. Fluid Mech.* **808**, 511–538.

DE GIOVANETTI, M., SUNG, H. J. & HWANG, Y. 2017 Streak instability in turbulent channel flow: the seeding mechanism of large-scale motions. *J. Fluid Mech.* **832**, 483–513.

HAMILTON, J. M., KIM, J. & WALEFFE, F. 1995 Regeneration mechanisms of near-wall turbulence structures. *J. Fluid Mech.* **287**, 317–348.

IUSO, G., ONORATO, M., SPAZZINI, P. G. & DI CICCA, G. M. 2002 Wall turbulence manipulation by large-scale streamwise vortices. *J. Fluid Mech.* **473**, 23–58.

JEONG, J. & HUSSAIN, F. 1995 On the identification of a vortex. *J. Fluid Mech.* **285**, 69–94.

JIMÉNEZ, J. & PINELLI, A. 1999 The autonomous cycle of near-wall turbulence. *J. Fluid Mech.* **389**, 335–359.

JUNG, W. J., MANGIAVACCHI, N. & AKHAVAN, R. 1992 Suppression of turbulence in wall-bounded flows by high-frequency spanwise oscillations. *Phys. Fluids* A **4** (8), 1605–1607.

KIM, J. 2011 Physics and control of wall turbulence for drag reduction. *Phil. Trans. R. Soc. Lond.* A **369** (1940), 1396–1411.

KIM, J. & BEWLEY, T. R. 2007 A linear systems approach to flow control. *Annu. Rev. Fluid Mech.* **39**, 383–417.

KLINE, S. J., REYNOLDS, W. C., SCHRAUB, F. A. & RUNSTADLER, P. W. 1967 The structure of turbulent boundary layers. *J. Fluid Mech.* **30** (04), 741–773.

LAIZET, S. & LAMBALLAIS, E. 2009 High-order compact schemes for incompressible flows: a simple and efficient method with quasi-spectral accuracy. *J. Comput. Phys.* **228** (16), 5989–6015.

LAIZET, S. & LI, N. 2011 Incompact3d: a powerful tool to tackle turbulence problems with up to $O(10^5)$ computational cores. *Intl J. Numer. Meth. Fluids* **67** (11), 1735–1757.

LEE, M. & MOSER, R. D. 2015 Direct numerical simulation of turbulent channel flow up to Re 5200. *J. Fluid Mech.* **774**, 395–415.

LI, Y. P., WONG, C. W., LI, Y. Z., ZHANG, B. F. & ZHOU, Y. 2014 Drag reduction of a turbulent boundary layer using plasma actuators. In *Proceeding of the 19th Australasian Fluid Mechanics Conference*, Australasian Fluid Mechanics Society.

https://doi.org/10.1017/jfm.2018.553 Published online by Cambridge University Press

MAHFOZE, O. & LAIZET, S. 2017 Skin-friction drag reduction in a channel flow with streamwise-aligned plasma actuators. *Intl J. Heat Fluid Flow* **66**, 83–94.

MAMORI, H., IWAMOTO, K. & MURATA, A. 2014 Effect of the parameters of traveling waves created by blowing and suction on the relaminarization phenomena in fully developed turbulent channel flow. *Phys. Fluids* **26** (1), 015101.

OLIVER, T. A., MALAYA, N., ULERICH, R. & MOSER, R. D. 2014 Estimating uncertainties in statistics computed from direct numerical simulation. *Phys. Fluids* **26** (3), 035101.

PARK, H., SUN, G. & KIM, C.-J. 2014 Superhydrophobic turbulent drag reduction as a function of surface grating parameters. *J. Fluid Mech.* **747**, 722–734.

QUADRIO, M. 2011 Drag reduction in turbulent boundary layers by in-plane wall motion. *Phil. Trans. R. Soc. Lond.* A **369** (1940), 1428–1442.

QUADRIO, M. & RICCO, P. 2004 Critical assessment of turbulent drag reduction through spanwise wall oscillations. *J. Fluid Mech.* **521**, 251–271.

QUADRIO, M., RICCO, P. & VIOTTI, C. 2009 Streamwise-travelling waves of spanwise wall velocity for turbulent drag reduction. *J. Fluid Mech.* **627**, 161–178.

RASTEGARI, A. & AKHAVAN, R. 2015 On the mechanism of turbulent drag reduction with super-hydrophobic surfaces. *J. Fluid Mech.* **773**, R4.

RASTEGARI, A. & AKHAVAN, R. 2018 The common mechanism of turbulent skin-friction drag reduction with superhydrophobic longitudinal microgrooves and riblets. *J. Fluid Mech.* **838**, 68–104.

REYNOLDS, W. C. & HUSSAIN, A. K. M. F. 1972 The mechanics of an organized wave in turbulent shear flow. Part 3. Theoretical models and comparisons with experiments. *J. Fluid Mech.* **54** (2), 263–288.

RICCO, P. & HAHN, S. 2013 Turbulent drag reduction through rotating discs. *J. Fluid Mech.* **722**, 267–290.

RICCO, P. & QUADRIO, M. 2008 Wall-oscillation conditions for drag reduction in turbulent channel flow. *Intl J. Heat Fluid Flow* **29** (4), 891–902.

ROTHSTEIN, J. P. 2010 Slip on superhydrophobic surfaces. *Annu. Rev. Fluid Mech.* **42**, 89–109.

SCHLATTER, P., LI, Q., ÖRLÜ, R., HUSSAIN, F. & HENNINGSON, D. S. 2014 On the near-wall vortical structures at moderate Reynolds numbers. *Eur. J. Mech. (*B*/Fluids)* **48**, 75–93.

SCHOPPA, W. & HUSSAIN, F. 1998 A large-scale control strategy for drag reduction in turbulent boundary layers. *Phys. Fluids* **10** (5), 1049–1051.

SCHOPPA, W. & HUSSAIN, F. 2002 Coherent structure generation in near-wall turbulence. *J. Fluid Mech.* **453**, 57–108.

SEGAWA, T., MIZUNUMA, H., MURAKAMI, K., LI, F.-C. & YOSHIDA, H. 2007 Turbulent drag reduction by means of alternating suction and blowing jets. *Fluid Dyn. Res.* **39** (7), 552–568.

SMITH, C. R. & METZLER, S. P. 1983 The characteristics of low-speed streaks in the near-wall region of a turbulent boundary layer. *J. Fluid Mech.* **129**, 27–54.

THOMAS, F., CORKE, T., HUSSAIN, F., DUONG, A., MCGOWAN, R., JASINSKI, C. & SIMMONS, D. 2016 Turbulent boundary layer drag reduction by active control of streak transient growth. In *Bulletin of the APS, 69th Annual Metting of the APS Division of Fluid Dynamics, Vol. 61, No. 20*, American Physics Society.

TOUBER, E. & LESCHZINER, M. A. 2012 Near-wall streak modification by spanwise oscillatory wall motion and drag-reduction mechanisms. *J. Fluid Mech.* **693**, 150–200.

WILLIS, A. P., HWANG, Y. & COSSU, C. 2010 Optimally amplified large-scale streaks and drag reduction in turbulent pipe flow. *Phys. Rev.* E **82** (3), 036321.

XI, C., HUSSAIN, F. & SHE, Z.-S. 2018 Quantifying wall turbulence via a symmetry approach. Part 2. Reynolds stresses. *J. Fluid Mech.* **850**, 401–438.

YAKENO, A., HASEGAWA, Y. & KASAGI, N. 2014 Modification of quasi-streamwise vortical structure in a drag-reduced turbulent channel flow with spanwise wall oscillation. *Phys. Fluids* **26** (8), 085109.

YAO, J., CHEN, X., THOMAS, F. & HUSSAIN, F. 2017 Large-scale control strategy for drag reduction in turbulent channel flows. *Phys. Rev. Fluids* **2**, 062601(R).

https://doi.org/10.1017/jfm.2018.553 Published online by Cambridge University Press